

# **Phase Field Modelling for Studying Microstructure Evolution**

*Project report submitted to  
Visvesvaraya National Institute of Technology, Nagpur  
in partial fulfilment of the requirements for the award of  
the degree*

**Bachelor of Technology  
In  
Metallurgical & Materials Engineering**

*By*

**Adesh Hatwar (BT18MME008) Aman Shende (BT18MME021)**

**Gudide Hareesh (BT18MME039) Sonali Bramhe (BT18MME082)**

under the guidance of

**Dr. Chaitanya A. Joshi**



**Department of Metallurgical & Materials Engineering  
Visvesvaraya National Institute of Technology  
Nagpur 440 010 (India)  
Year 2021/22**

# **Phase Field Modelling for Studying Microstructure Evolution**

*Project report submitted to  
Visvesvaraya National Institute of Technology, Nagpur  
in partial fulfilment of the requirements for the award of  
the degree*

## **Bachelor of Technology In Metallurgical & Materials Engineering**

*By*

**Adesh Hatwar (BT18MME008) Aman Shende (BT18MME021)**

**Gudide Hareesh (BT18MME039) Sonali Bramhe (BT18MME082)**

under the guidance of

**Dr. Chaitanya A. Joshi**



**Department of Metallurgical & Materials Engineering  
Visvesvaraya National Institute of Technology  
Nagpur 440 010 (India)  
Year 2021/22**

© Visvesvaraya National Institute of Technology (VNIT) 2022



## **Declaration**

We, Adesh, Aman, Hareesh, Sonali hereby declare that this project work titled “**Phase Field Modelling for Studying Microstructure Evolution**” is carried out by us in the Department of **Metallurgical & Materials Engineering** of Visvesvaraya National Institute of Technology, Nagpur. The work is original and has not been submitted earlier whole or in part for the award of any degree/diploma at this or any other Institution / University.

Adesh Hatwar (BT18MME008)

Aman Shende (BT18MME021)

Gudide Hareesh (BT18MME039)

Sonali Bramhe (BT18MME082)

Date:

## **Certificate**

This to certify that the project titled “**Phase Field Modelling for Studying Microstructure Evolution**”, submitted by Adesh, Aman, Hareesh, Sonali in partial fulfillment of the requirements for the award of the degree of **Bachelor of Technology in Metallurgical & Materials Engineering**, VNIT Nagpur. The work is comprehensive, complete and fit for final evaluation.

**Dr. Chaitanya A. Joshi**

Assistant Professor, MME, VNIT, Nagpur

**Dr. Jatin G. Bhatt**

Head, Department of **Metallurgical & Materials Engineering**

VNIT, Nagpur

Date:

## **ACKNOWLEDGEMENT**

Finishing a piece of work can never be a single person's effort. It is often the effort and contribution of the number of individuals in a direct or indirect manner. We think it might not be possible for us to complete the thesis without these people. We thereby, convey our feelings to all those personalities who have helped us along the way.

We would like to express our deepest gratitude and warmest thanks to our esteemed supervisor Dr. C. A. Joshi for his patience, motivation, support and enthusiasm. We have benefited greatly from his immense wealth of knowledge and meticulous editing. His invaluable advice and timely suggestions at pivotal stages have made it possible for us to complete this work. Also, we would like to thank the Head of Department, Dr. J. G. Bhatt for his able guidance and for providing all the necessary facilities, which were indispensable in the completion of this project.

We owe a special thanks to Dr. Ajeet Kumar Srivastav for his guidance, valuable suggestions and helpful discussions. We are grateful to our Parents for providing us the opportunity and exposing us to the world of knowledge. We thank our family for their love, support and constant encouragement.

## **Abstract**

Simulation is a powerful tool for the analysis of new system designs, retrofits to existing systems and proposed changes to operating rules. This thesis provides an introduction to Phase Field modelling for studying microstructure evolution. After this we have discussed theory related to Phase Field equations and simulations and further, we have plotted the microstructure evolution by Phase Field simulation using the Cahn-Hilliard equation. In this particular project two simulations are plotted:

- 1) General binary phase diagram
- 2) Spinodal decomposition in 2D.

Thereafter, we have discussed the result obtained. After this we have studied various research papers regarding Phase Field Modelling in terms of solidification, grain growth and its application in rechargeable batteries and irradiated nuclear materials.

## List of Figures

Figure 1. $\Delta G_{\text{mix}}$ at various temperature	5
Figure 2. Diffusion of A and B atoms in non-phase separating alloy	8
Figure 3. Diffusion of A and B atoms in phase separating alloy	9
Figure 4. Spinodal decomposition	10
Figure 5. Free energy v/s composition diagram	11
Figure 6. First-order derivative of free energy v/s composition diagram $G'$	11
Figure 7. Second-order derivative of free energy v/s composition diagram $G''$	12
Figure 8. Free energy curve for spinodal region	12
Figure 9. Free energy curve	13
Figure 10. Miscibility gap separated by spinodal line	14
Figure 11. Explaining spinodal	15
Figure 12. Result obtained after running code 1	17
Figure 13(a). Initial Microstructure for mesh size of 64 x 64	21
Figure 13(b). Evolved Microstructure for mesh size of 64 x 64	21
Figure 14(a). Initial Microstructure for mesh size of 250 x 250	22
Figure 14(b). Evolved Microstructure for mesh size of 250 x 250	22
Figure 15. Evolved microstructure in 3D	23

Figure 16. Dendritic Microstructure & Non-Dendritic Microstructure	26
Figure 17. Binary phase diagram of Al-7Si-0.3 Mg alloy	26
Figure 18. Simple lens type phase Diagram (Initial at temperature a → b (undercooled to 20K) → c (temperature raised) → d (undercooled))	27
Figure 19. Dendrite with primary and secondary arms	27
Figure 20. Phase Field simulation of dendritic to globular transition: (a) Fully developed dendrite; (b) Remelting of dendrite at position c in above Fig.; (c, d) Solidifying at lower temperature at position d (start of globularization)	28
Figure 21. Phase profile of Ti-6Al-4V at different temperature gradient (a) 2222.72°C mm <sup>-1</sup> , (b) 2294.13°C mm <sup>-1</sup> , (c) 2506.12°C mm <sup>-1</sup> and (d) 2822.77°C mm <sup>-1</sup>	31
Figure 22. Variation of columnar dendritic spacing with temperature gradient	31
Figure 23. Variation of width of dendritic arm with temperature gradient.	32
Figure 24. Phase profile at different scan speed (a) 200 mm s <sup>-1</sup> (b) 400 mm s <sup>-1</sup> (c) 600 mm s <sup>-1</sup> (d) 800 mm s <sup>-1</sup> (e) 1000 mm s <sup>-1</sup>	32
Figure 25(a). Columnar dendritic spacing with scan speed.	33
Figure 25(b). Width of dendrite arms with scan speed.	33
Figure 26. (a) Simulated phase profile (b) microstructure of Ti-6Al-4V.	34
Figure 27. Columnar dendritic spacing vs. temperature gradient.	34
Figure 28. 2D section of microstructures after (a)1000, (b) 2000, (c) 4000 iterations.	36
Figure 29. Grain size distribution data	36
Figure 30. Time evolution of the average grain size	36

Figure 31. (a)2D section of initial microstructure of simulation. (b) grain boundary energies to each kind of boundaries	37
Figure 32. 2D section of microstructure evolution after 4000 iterations with decreasing percentages of type I grains.	38
Figure 33. Time evolution of average grain size	38
Figure 34. TEM image and simulated image of precipitates in Al-Cu alloy	40
Figure 35. Twinning in Magnesium	41
Figure 36. Experimental and simulated martensite	42
Figure. 37 Crack propagation during the de-lithiation process.	46
Figure. 38 Phase Field simulations of Li dendrite growth. Evolution of an order parameter, b Li+ concentration, c electric potential.	47
Figure 39. Scanning electron microscope (SEM) image of gas bubble structure in UO <sub>2</sub>	48
Figure 40. Effect of tensile stress on helium gas bubble structure in Fe-17wt% Cr-17wt% Ni after annealing at 1023K for 60 h	49
Figure 41. Effect of grain morphology on gas bubble swelling kinetics under given fission rate $\dot{\rho} = 1.4 \times 10^{22} \text{ fission/m}^3\text{s}$ and nucleation factor $f_n = 0.02$ . Crystals A and B have average grain sizes of 1.34 $\mu\text{m}$ , and 4.36 $\mu\text{m}$ , respectively. Crystals B, C, and D have the similar average grain volume but different aspect ratios 1:1, 4:1, and 16:1	50

## Nomenclature

1. Fig: Figure
2. GNU: GNU's Not Unix
3. DFT: Discrete Fourier Transform
4. RB: Rechargeable Batteries
5. SEI: Solid Electrolyte Interphase Layer
6. PF: Phase Field
7. FP: Function Point oriented estimation mode



# INDEX

1. Introduction	1
1.1 Software and Tools	2
2. Phase Field Models	3
2.1 Chemical Potential	6
2.2 Spinodal Decomposition	10
2.3 Coding and Simulations	16
2.3.1 Spinodal Region in phase diagram	16
2.3.2 Spinodal Decomposition in 2D	17
3. Result and Discussion	21
4. Other applications of Phase Field modelling	24
4.1 Experimental studies and Phase Field modelling of microstructure evolution during solidification with electromagnetic stirring	25
4.2 Phase Field simulation of microstructure evolution of Ti–6Al–4V in electron beam additive manufacturing process	29
4.3 Phase Field Model simulation of grain growth in three dimensions under isotropic and anisotropic grain boundary energy conditions	35
4.4 Phase Field modelling of microstructure evolution: Recent applications, perspectives and challenges	39
4.5 Application of the Phase Field method in rechargeable batteries	43
4.6 Applications of the Phase Field method in predicting microstructure and property evolution of irradiated nuclear materials	48
5. Conclusion	51
6. References	52

# **Chapter 1 - INTRODUCTION**

Mathematics is used to analyse a variety of situations and occurrences. It is increasingly being used to solve real-world problems. Numerical methods and computer algorithms can solve complex and lengthy problems with ease. A better representation and solution of certain problems can be obtained by translating a real-life problem into a mathematical form. Thus, a mathematical model describes a phenomenon using a set of mathematical equations that are solved to obtain parameters of interest using numerical methods, which are commonly performed by a computer program. The study of how the model reacts to external factors is known as simulation. Models are subjected to inputs and constraints that imitate the real-world events during simulations. Simulation is crucial because it can be carried out in hostile environments that cannot be replicated in laboratories, such as extreme high pressures or high temperatures.

Computational materials science aims for a better understanding of the properties and phenomena of materials so that better materials can be developed for varied uses and critical applications. The advancement in materials science is attributed to the ability to exploit and engineer new materials for certain required properties. Microstructure plays a critical role in influencing properties of a material. Microstructure modelling and simulation helps in understanding the connection between microstructure and processing parameters. Hence, we will be studying microstructure evolution by a modelling method known as the Phase Field modelling.

Phase Field modelling is a technique for simulating mesoscale microstructure evolution. Mesoscopic means intermediate hence, mesoscale is the intermediate between microscopic and macroscopic scale. Without explicitly monitoring the positions of interfaces, the Phase Field technique can deal with the evolution of complex microstructures. Phase Field models have been successfully applied to various materials processes like solidification, solid-state phase transformations, precipitate growth and coarsening, martensitic transformations, nucleation and grain growth.

After discussing the applications of Phase Field models, the software and tools which are used for modelling and simulation are discussed in the next part.

## **1.1] Software and Tools**

Octave: GNU Octave is a high-level language, primarily intended for numerical computations. It provides a convenient command line interface for solving linear and nonlinear problems numerically, and for performing other numerical experiments using a language that is mostly compatible with MATLAB. It may also be used as a batch-oriented language.

Octave has extensive tools for solving common numerical linear algebra problems, finding the roots of nonlinear equations, integrating ordinary functions, manipulating polynomials, and integrating ordinary differential and differential-algebraic equations. It is easily extensible and customizable via user-defined functions written in Octave's own language, or using dynamically loaded modules written in C++, C, Fortran, or other languages.

After this Chapter 2 discusses the Phase Field models theoretically. Chapter 3 explains implementation in terms of coding and simulations. Chapter 4 explores several other applications of Phase Field modelling in different areas. Chapter 5 is about concluding remarks about the project and then Chapter 6 includes references.

## Chapter 2 - PHASE FIELD MODELS

When we add two different types of atoms together, there are possibilities that these atoms may form random solid solutions, phase separated solid solutions or ordered solid solutions.

These can be studied by a regular solution model [1] as what happens when different atoms are put together.

This regular model is studied based on Gibbs free energy.

The Gibbs formula is:

$$G = H - TS$$

Where H is Enthalpy

T is temperature

S is entropy

And in condensed systems that are solid and liquid, the enthalpy is approximated as Internal Energy.

The Gibbs formula for the condensed phases becomes

$$G \sim U - TS$$

Suppose we take two atoms A and B and put them together to form the Binary alloy.

If we assume that this forms the ideal solution then

$$\Delta G_{\text{mix}} = \Delta U_{\text{mix}} - T\Delta S_{\text{mix}}$$

And  $\Delta U_{\text{mix}} = 0$  is zero for the ideal solutions as it does not distinguish between A-A, A-B or B-B bonds.

The new equation becomes

$$\Delta G_{\text{mix}} = -T\Delta S_{\text{mix}}$$

$$\Delta G_{\text{mix}} = R T [X_A \ln X_A + X_B \ln X_B] \quad \dots \text{eq. 2.1}$$

Where, R = Universal gas constant

T = temperature

$X_A$  = mole fraction of A atoms

$X_B$  = mole fraction of B atoms

The equation 2.1 always gives negative values as homogeneous mixing of atoms (random solid solution) takes place which has lower free energy.

But if we take a regular solution model, then it distinguishes between A-A, B-B and A-B bonds.

And  $\Delta H_{mix}$  does not become zero and has some value.

$$\Delta G_{mix} = \Omega X_B (1 - X_B) + RT [(X_B) \log (X_B) + (1 - X_B) \log (1 - X_B)] \dots \text{eq. 2.2}$$

Where  $\Omega$  is a regular solution parameter which depends on bond energy

In equation 2.2, if Temperature (T) is high, the entropy term will be dominant and it is always negative and hence Gibbs free energy will be always negative and the system will prefer a random solid solution.

But at lower Temperature values  $\Omega X_B (1 - X_B)$  term will play a significant role. If  $\Omega$  has negative then ordered solution forms and if  $\Omega$  is positive then phase separated solid solution forms.

The above discussion can be explained graphically. So, equation 2.2 is plotted first by individual terms that are  $\Delta H_{mix}$  and  $\Delta S_{mix}$  shown in figure 1.

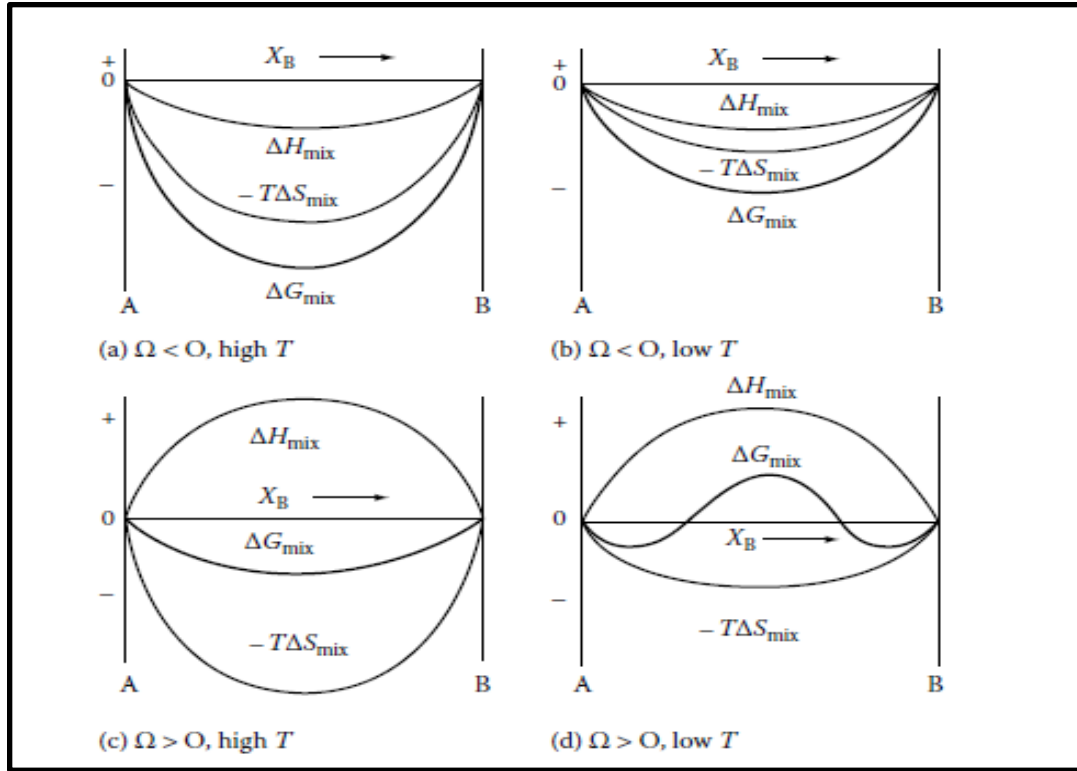


**Figure 1  $\Delta G_{mix}$  at various temperature [1]**

In figure 1, a) and c) are drawn for higher temperatures in which the entropy term is dominant and hence whatever the sign of  $\Omega$ , Gibbs free energy is negative and the system prefers to form random solid solutions.

Figure 1, b) and d) are with relatively low temperatures where the entropy term is not dominant. In these cases, if the  $\Omega$  sign is negative then enthalpy becomes negative means A-B bonds are preferred than A-A and B-B bonds and ordered solution forms ( $\Omega = E_{AB} - 1/2 (E_{AA} + E_{BB})$ ).

$\Omega$  sign is positive means A-A and B-B bonds are preferred than A-B bonds and phase separated solid solution forms which can be seen from the figure also than Gibbs free energy of A-B bonds is higher than A-A and B-B phase separated solution.

So, from the above discussion we have said that at higher temperature entropy dominates and random solid solution forms and at lower temperatures ordered or phase separation may take place.

But if we consider the Fick's first law, it says that whenever the system has a concentration gradient, the system tries to minimise it but the opposite is happening in this case.

The above problem is explained by Cahn and Hilliard. [1]

Fick's first law of diffusion is not valid in every situation. Concentration gradient exists in some systems and diffusion does not happen to reduce it. Hence further section explores about chemical potential.

## 2.1 Chemical Potential

The chemical potential of a component  $i$  is a measure of change of free energy of a system with respect to the addition or removal of atoms of that component in the system, when temperature, pressure and other components are kept constant.

Chemical potential ( $\mu$ ) is partial molar Gibbs Free Energy.

$$\mu = \partial G / \partial n_i$$

Consider a system with phase C and D in equilibrium. It consists of components A and B. Temperature and Pressure of phases C and D is constant.

The total Gibbs Free Energy of the system is the sum of free energy of phases C and D.

$$G = G^C + G^D \quad \dots \text{eq. 2.3}$$

Where  $G$  is the free energy of the system,  $G^C$  and  $G^D$  are the free energies of phases C and D respectively.

Now, move some small no. of atoms A from phase D to C. C phase is gaining some amount of A and phase D is losing that same amount of A. This is represented in the form of equations 2.4 and 2.5.

$$dn_A^C = dn_A \quad \dots \text{eq. 2.4}$$

$$dn_A^D = - dn_A \quad \dots \text{eq. 2.5}$$

where,  $dn_A$  is the change in amount of A.  $dn_A^C$  and  $dn_A^D$  are the changes in amount of A in phases C and D respectively.

This change results in a change in free energy of both phases. Since the phases are in equilibrium with one another free energy of the system remains the same. Therefore, the change in free energy of the system is zero when  $dn_A$  is moved from phase D to C, which is given by the following equation

$$\Rightarrow dG^C + dG^D = 0$$

Rewriting with the help of the fundamental equation of  $dG = -SdT + VdP + \mu dn$

$$\therefore (-S^C dT + V^C dP + \mu_A^C dn_A^C + \mu_B^C dn_B^C) + (-S^D dT + V^D dP + \mu_A^D dn_A^D + \mu_B^D dn_B^D) = 0 \dots \text{eq. 2.6}$$

Since Temperature and Pressure of both phases is constant, the terms  $dT$  and  $dP$  will become zero.

$$(-S^C dT + V^C dP + \mu_A^C dn_A^C + \mu_B^C dn_B^C) + (-S^D dT + V^D dP + \mu_A^D dn_A^D + \mu_B^D dn_B^D) = 0$$

$$\Rightarrow \mu_A^C dn_A^C + \mu_A^D dn_A^D = 0$$

Rewriting above using eq. 2.4 and 2.5

$$\therefore \mu_A^C dn_A + \mu_A^D (-dn_A) = 0$$

$$\Rightarrow (\mu_A^C - \mu_A^D) dn_A = 0$$

For above equation to be zero the difference should be zero, which requires

$$\Rightarrow \mu_A^C = \mu_A^D$$

If a system is in equilibrium the chemical potential of a component is equal in the two phases of the system.

To understand the importance of Chemical Potential in Diffusion let us see an example.



It is seen in the Iron-Carbon Phase Diagram that as austenite cools below the eutectoid temperature, Pearlite is formed which is a lamellar mixture of alpha ferrite and cementite. At the eutectoid temperature the solubility of carbon is 0.025% in alpha ferrite. Cementite is a compound with 6.67% carbon by weight. The carbon content in cementite is much higher than that of the carbon content in ferrite phase. However, diffusion of carbon does not occur from cementite to ferrite, despite its concentration gradient between cementite and ferrite. Ferrite and cementite remain as two separate entities in pearlite. This is attributed to the reason that the chemical potential of carbon is the same in ferrite and cementite.

Chemical Potential is the quantity which decides which path atoms will move and that till it gets equalised there will be movement of atoms.

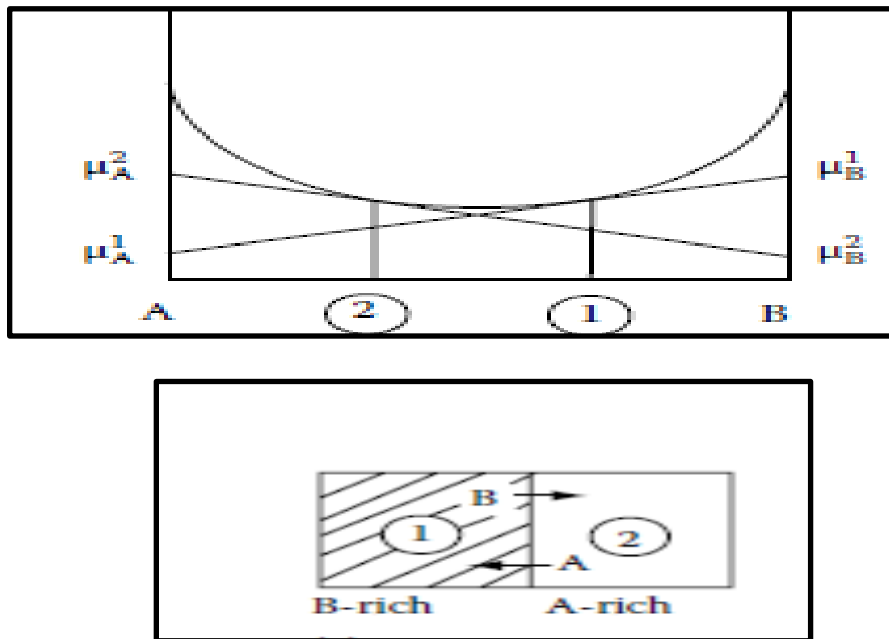


**Figure 2 Diffusion of A and B atoms in non-phase separating alloy [2]**

In figure.2, if we take two different alloys 1 and 2 rich in B and A respectively and draw the common tangent to its respective Gibbs free energy curve then can see that for alloy 1,  $\mu_B$  is higher than  $\mu_B$  and for alloy 2,  $\mu_A$  is higher than  $\mu_A$ . Hence, atoms of B will move from alloy 1 and A will move from alloy 2 when these alloys are welded together.

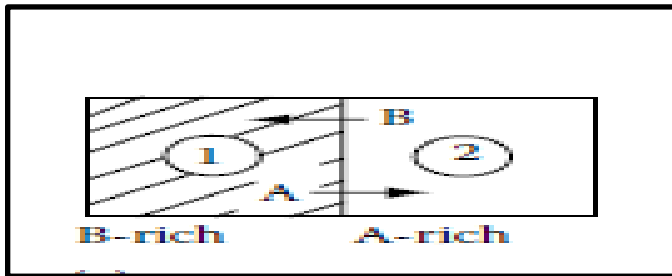
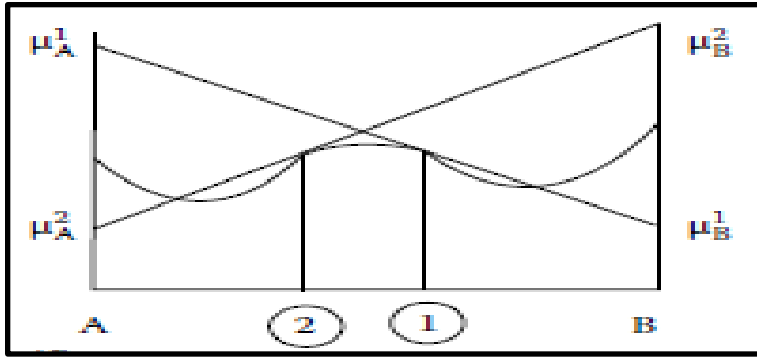


**Figure 3 Diffusion of A and B atoms in phase separating alloy [2]**

In figure.3, if we take two different alloys 1 and 2 rich in B and A respectively and draw the common tangent to its respective Gibbs free energy curve then can see that for alloy 1,  $u_{B1}$  is lower than  $u_{B2}$  and for alloy 2,  $u_{A2}$  is lower than  $u_{A1}$ . Hence, atoms of A will move from alloy 1 and B will move from alloy 2 when these alloys are welded together and they phase separate.

Hence Fick's law of diffusion is invalid for phase separating systems

$$J = -D \, dc/dx$$

Therefore, modified Diffusion equation is

$$J = -M \, du/dx$$

Where  $u$  is chemical potential,  $M$  is mobility

## 2.2 Spinodal Decomposition

Spinodal Decomposition takes place via the Spinodal mechanism and not by using nucleation and growth. In nucleation and growth mechanism composition of the two different phases try to minimise the concentration gradient but in the case of spinodal decomposition concentration gradient increases because this helps in lowering the free energy. [1]

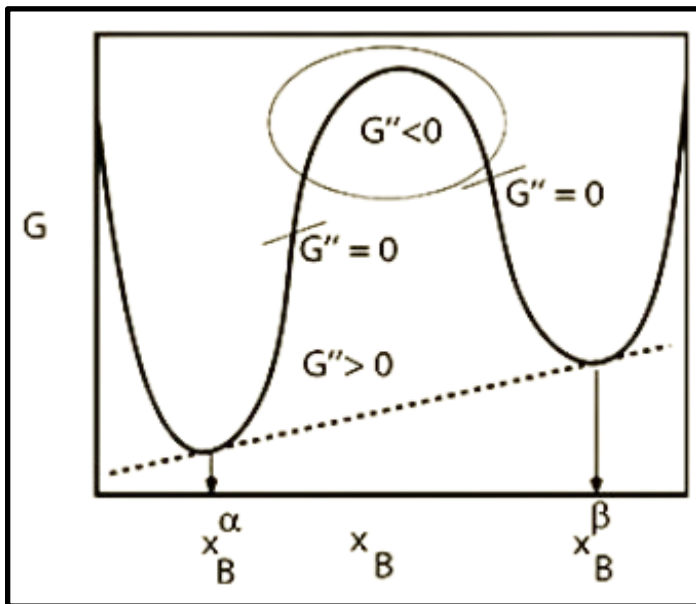
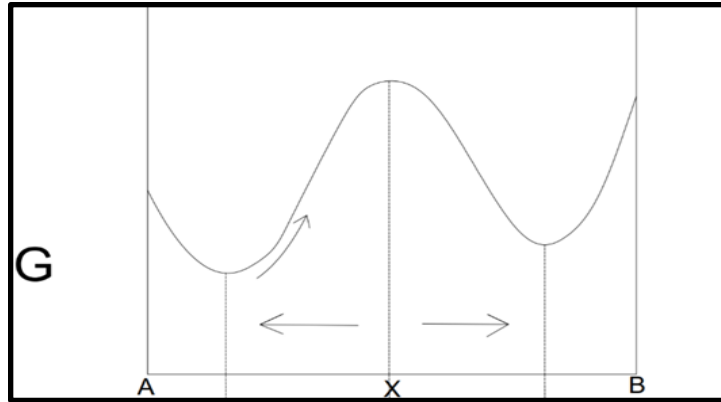


Figure 4 Spinodal decomposition [1]

### Free-energy Diagram of spinodal decomposition:

The phase transition of spinodal decomposition can be illustrated with a phase diagram that displays a miscibility gap (see figure 4). In this way, phase separation occurs when a material moves into the unstable region of the phase diagram. Spinodal regions always exist between binodal points, identified by going through free-energy curves to determine where the curvature is negative. At the critical point, the binodal and spinodal meet. Spinodal decomposition occurs when a material is moved into the spinodal region of the phase diagram.



**Figure 5 Free energy v/s composition diagram**

Spinodal decomposition occurs when the second derivative of the free energy vs composition diagram has negative curvature. We draw the graph of first free energy vs composition (see figure 5), next we draw the first derivative of free energy vs composition graph (see figure 6), next we draw the second derivative of free energy vs composition curve (see figure 7)

Positive arch (nucleation) and negative arch (spinodal) regions of the free energy versus composition diagram.

At zero, the curvature value of Gibbs free energy mechanism of phase separation by nucleation changes to spinodal.

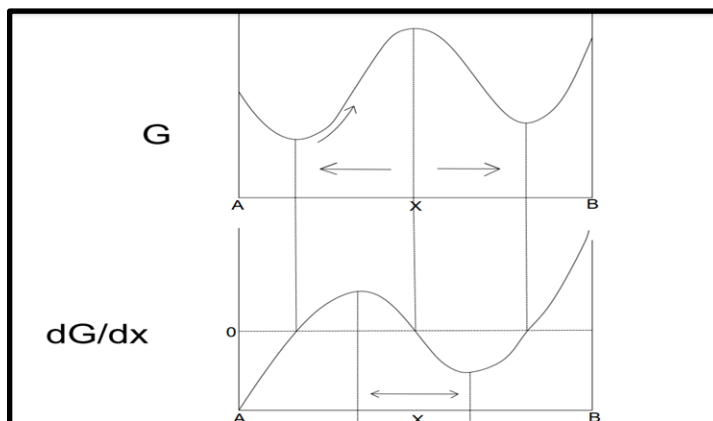


**Figure 6 First-order derivative of free energy v/s composition diagram  $G'$**

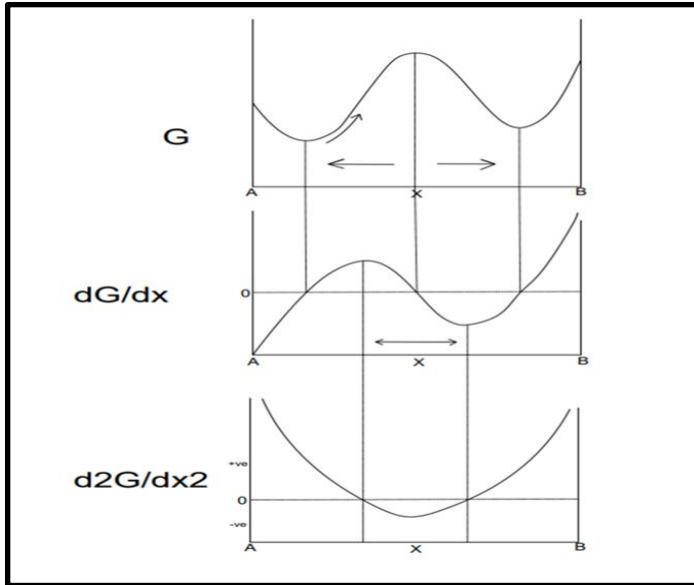


**Figure 7 Second-order derivative of free energy v/s composition diagram  $G''$**

We have the spinodal decomposition in between two binodal points. Here we have two spinodal points where  $G'' = 0$ , and the regions within those points are spinodal decomposition regions ( $G'' < 0$ ).

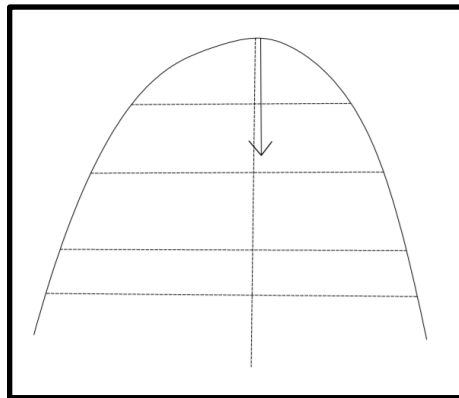


**Figure 8 Free energy curve for spinodal region**

Spinodal decomposition occurs in an unstable state, while nucleation occurs in a stable state. The moment when you take any composition it would likely split into two phases of different composition.

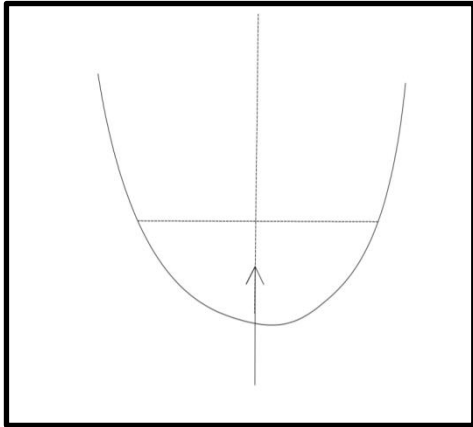


**Figure 9 Free energy curve**

Here in the case of the spinodal region the free energy is decreasing (see figure 8). But in the case of the nucleation region we can see increasing free energy beyond the spinodal region (see figure 9).

Phase Field approach is an effective tool for simulations of microstructure development and evolution at the "mesoscale" because of its universality and ease of implementation.

In an alloy system, the creation of the phase is normally carried out by a nucleation mechanism, growth mechanism, or spinodal degradation mechanism. Phase Field approach may be used to analyse these three processes, and the findings can be compared to basic phase conversion theories such as Cahn Hilliard Spinodal decomposition theory and Lifshitz-Slyozov-Wagner (LSW) diffusion control. The phase composition caused by the spinodal degradation mechanism is different from phase separation. In contrast, nucleation and growth phase formation predict that the formed phase has a composition very close to the balance from the start of phase conversion. Furthermore, spinodal degradation is usually connected to the presence of a mixing gap in a balanced state diagram as shown in figure below. The miscibility gap is the equilibrium line, and there is only one phase in the composition and temperature above this line, but there is a mixture of two different phases in the miscibility gap. When the supersaturated  $\alpha$  phase is heated to a temperature higher than the miscibility gap, it is spinodal decomposed into a mixture of A-rich  $\alpha_1$  phase and B-rich  $\alpha_2$  phase of alloy

composition, and then quenched and heated or aged at a temperature lower than the chemical spinodal. The miscibility gap in figure 10 is usually associated with the free energy vs. composition plot. This figure shows how the shape of the free energy curve changes as the temperature drops. This type of curve, known as the spinodal curve, indicates that the alloy composition is in an unstable state and is expected to decompose into a mixture of A-rich  $\alpha_1$  phase and B-rich  $\alpha_2$  phase. The minimum and minimax points of the spinodal curve at each temperature correspond to the equilibrium and chemical spinodal curves shown in figure 10.

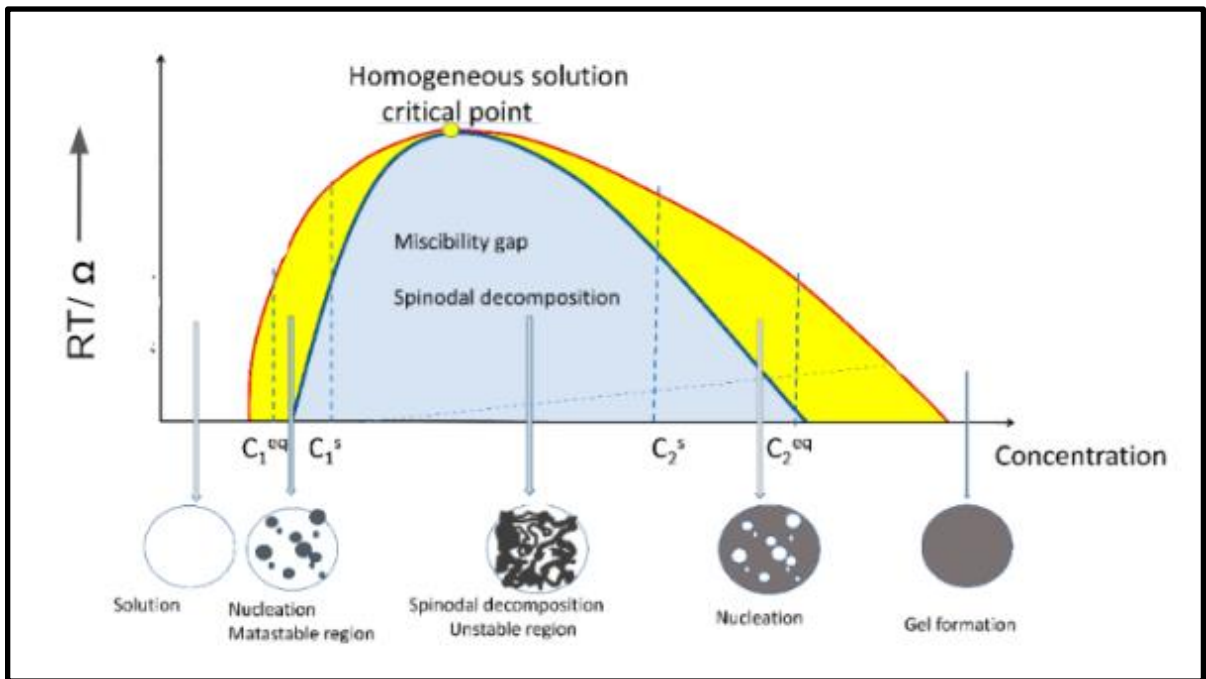


**Figure 10 Miscibility gap separated by spinodal line.**

As a special case of phase transformation, spinodal decomposition can be represented by a phase diagram. Spinodal decomposition can be represented by a phase diagram as a specific example of phase transformation. There is a miscibility gap (see figure 11). When a material moves into the unstable zone of the phase diagram, phase separation occurs. The boundary of the unstable region, sometimes referred to as the binodal or coexistence curve, is found by performing a common tangent construction of the free-energy diagram. The spinodal is an area within the binodal that may be determined by calculating where the free-energy curve's curvature is negative. The binodal and spinodal meet at the critical point. Spinodal decomposition takes place when a material enters the spinodal zone of the phase diagram.

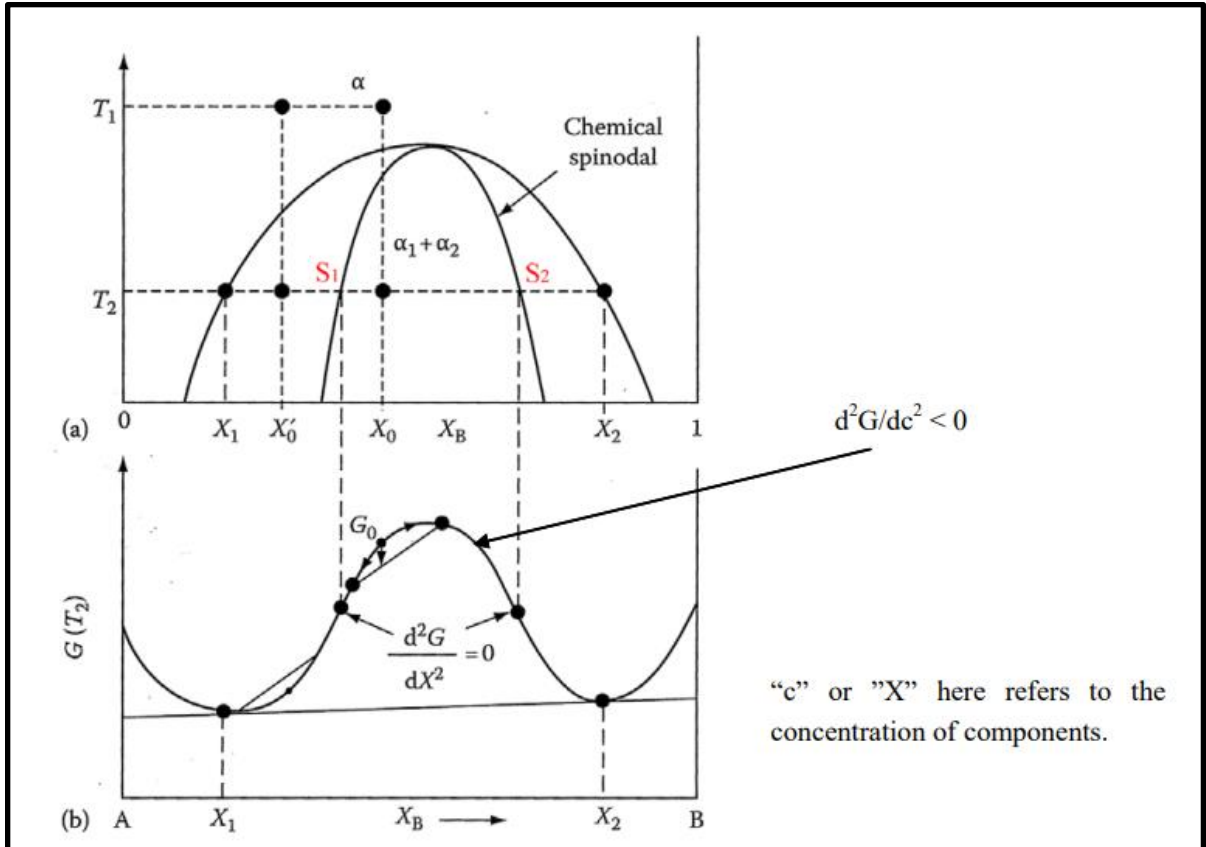


**Figure 11 Explaining spinodal**

The free energy curve is plotted as a function of composition for the phase separation temperature  $T_2$ . The phase compositions that correspond to the free energy minima are known as equilibrium phase compositions. Regions of negative curvature ( $d^2G/dc^2 < 0$ ) lie within the inflection points of the curve ( $d^2G/dc^2 = 0$ ) which are called the spinodes (as marked as  $S_1$  and  $S_2$  in the diagram above). For compositions within the spinodal, a homogeneous solution is unstable against microscopic fluctuations in density or composition, and there is no thermodynamic barrier to the growth of a new phase, i.e., the phase transformation is solely diffusion controlled.



## 2.3 Coding and Simulations

### 2.3.1 Code 1: Spinodal Region in phase diagram

Code for plotting Phase Diagram and inside of that the spinodal.

```
>> function y = G(a,x)
    y = a.*x.*(1.-x) .+ x.*log(x) .+ (1.-x) .*log(1.-x);
endfunction

>> x=0.001:0.001:0.999;
>> a(1) =2.0;
>> for i =1:400
    c(i) = fminbnd(@(x) G(a(i),x),0.001,0.499,optimset('TolX',1.e-12));
    d(i) = fminbnd(@(x) G(a(i),x),0.501,0.999,optimset('TolX',1.e-12));
    a(i+1) = a(i) + 0.01;
endfor

>> function z = Gpp(a,x)
    z= -2*a .+ 1./x .+ 1./(1.-x);
endfunction

>> a(1) = 2.01;
>> x0 = [0.0001;0.5001];
>> x1 = [0.4999;0.9999];
>> for i = 1:400
    f(i) = fzero(@(x) Gpp(a(i),x),x0);
    g(i) = fzero(@(x) Gpp(a(i),x),x1);
    a(i+1) = a(i) + 0.01;
endfor

>> for i = 1:400
    b(i)=a(i);
endfor
```

```
>> plot(f,1./b,g,1./b)
>> hold on
>> plot(c,1./b,d,1./b)
```

When we run the above code, we get the following image(region).

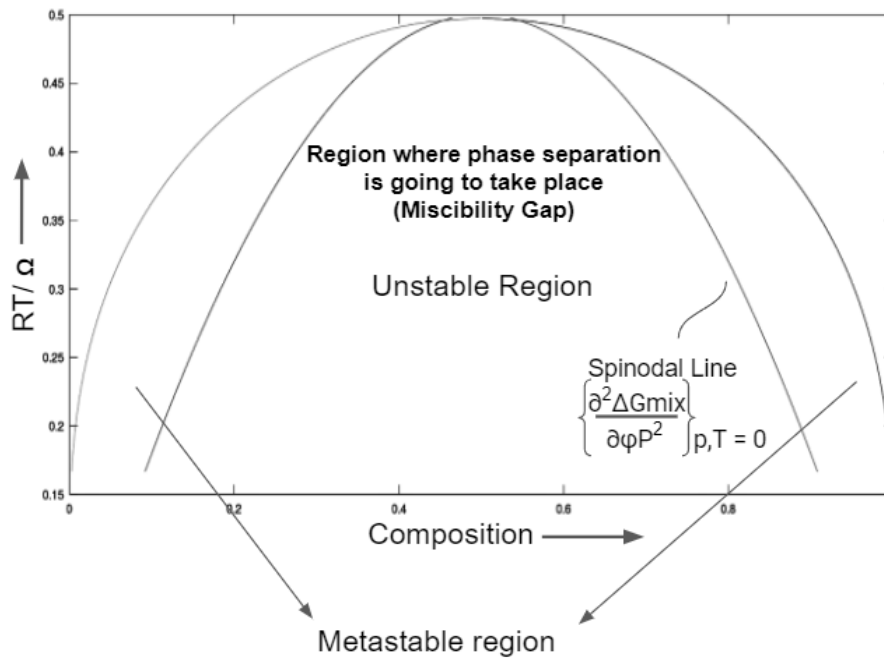


**Figure 12 Result obtained after running code 1.**

Figure 12 shows a miscibility gap having metastable and unstable regions which are separated by spinodal line.

### 2.3.2 Spinodal decomposition in 2D

Steps involved in Phase Field modelling:

1. Identifying the order parameter, that is composition. Its purpose is to decide the description of microstructure that is geometric description or topology.
2. Thermodynamic description for given microstructure - We write here the free energy functional because free energy is a function of composition and gradient in composition that is our order parameter.
3. Writing the evolution equation from Phase Field equation.

$$G/N_V = \int f_0(c) + k |\nabla|^2 dv \dots\dots\dots(\text{Phase Field eq})$$

where,  $f_0(c)$  is a function  $A c^2(1-c)^2$ .

Writing the Cahn-Hilliard Equation,

$$\frac{\partial c}{\partial t} = M * (\nabla)^2 * \mu = M * (\nabla)^2 * \frac{\partial(G/N_V)}{\partial c} = M * (\nabla)^2 * \left[ \frac{\partial(f_0)}{\partial c} - 2k (\nabla)^2 c \right]$$

$$\frac{\partial c}{\partial t} = M(\nabla)^2 g(c) - 2kM(\nabla)^4 c$$

Where, M is mobility

$\mu$  is chemical potential

$g(c)$  is  $\partial(f_0)/\partial c - 2k (\nabla)^2 c$

4. Solving the above equation in terms of composition (order parameter).

$$\tilde{c}^{t+\Delta t} = \frac{\tilde{c}^t - M(k_x^2 + k_y^2) \Delta t \tilde{g}}{1 + 2kM(k_x^2 + k_y^2) \Delta t}$$

## Code 2

Code for the spinodal decomposition in 2D. The code is fairly short, and implemented using semi-implicit Fourier spectral technique in which the periodic boundary condition is implicitly assumed. We have chosen a square domain(mesh) as per our required size which represents the region and this is where we are going to evolve our microstructure.

- more off
- Nx=250;
- Ny=250;
- for i=1:Nx
- for j=1:Ny
- $c(i,j) = 0.5 + 0.1*(0.5-\text{rand}());$
- endfor
- endfor

We start with an initial profile with a composition of about 0.5 with some noise. We choose these initial profile values because this is where the unstable region exists. This initial profile is going to evolve further into phase separated regions. Here,  $c(i,j)$  represents composition.

- `mesh(c);`
- `view(2);`
- `pause(0)`

Above line of codes are used for viewing the output that is our microstructure from top.

- `dt=0.5;`
- `halfNx= Nx/2;`
- `halfNy= Ny/2;`
- `delkx = 2*pi/Nx;`
- `delky = 2*pi/Ny;`
- `A=1.0;`
- `M=1.0;`
- `kappa=1.0;`

Above line of codes are used for implementing the periodic boundary conditions. And A, M, kappa are the constants.

- `for m=1:10`
- `for n=1:20`
- `g = 2.*A.*c.*(1.-c).*(1.-2.*c);`
- `ghat = fft2(g);`
- `chat = fft2(c);`
- `for i=1:Nx`
- `if((i-1) <= halfNx) kx = (i-1)*delkx;`
- `endif`

- `if((i-1) > halfNx) kx = (i-1-Nx)*delkx;`
- `endif`
- `for j=1:Ny`
- `if((j-1) <= halfNy) ky = (i-1)*delky;`
- `endif`
- `if((j-1) > halfNy) ky = (j-1-Ny)*delky;`
- `endif`
- `k2 = kx*kx + ky*ky;`
- `k4 = k2*k2;`
- `chat(i,j) = (chat(i,j) - M*dt*k2*ghat(i,j))/(1.+2*M*kappa*k4*dt);`
- `endfor`
- `endfor`
- `c=real(fft2(chat));`
- `endfor`
- `c=real(ifft2(chat));`
- `endfor`
- `mesh(c);`
- `view(2);`
- `pause(0);`

In the above lines of code, we are performing the simulation by evolving our microstructure. It involves calculating the value of  $G$  and then we take the Fourier transform. Once in every 20 steps we are viewing our microstructure that is inside out for loop in line 21 we are displaying our microstructure and see it evolving. Functions `fft2` and `ifft2` indicate that it is 2-Dimensional Fourier transformation. When the code executes completely, we get our final evolved microstructure.

### Chapter 3 - Result and Discussion

After running code 2 we get the following result for different mesh sizes:

- Small Mesh Size of 64 x 64

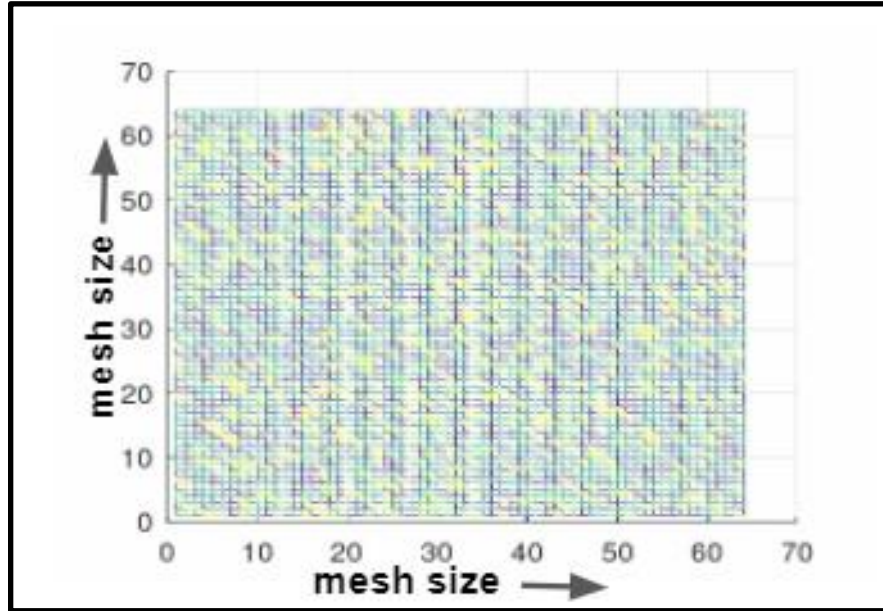


Figure 13(a) Initial Microstructure for mesh size of 64 x 64

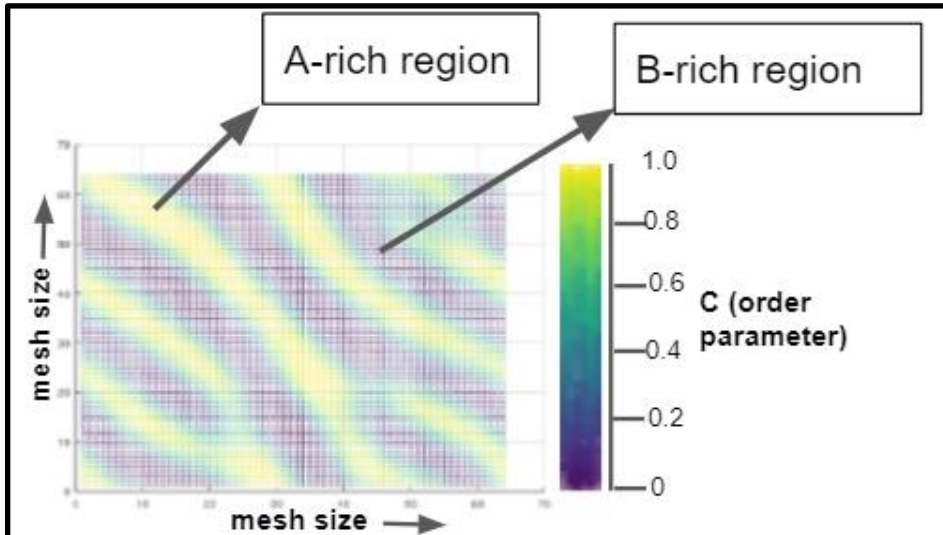
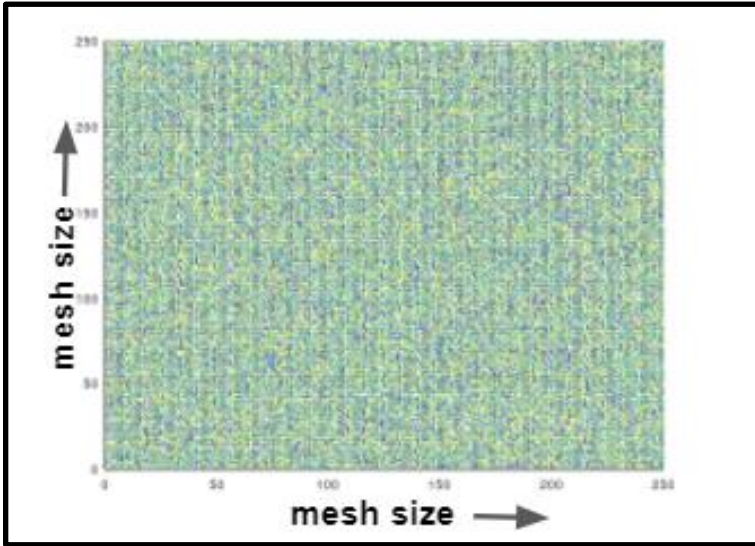
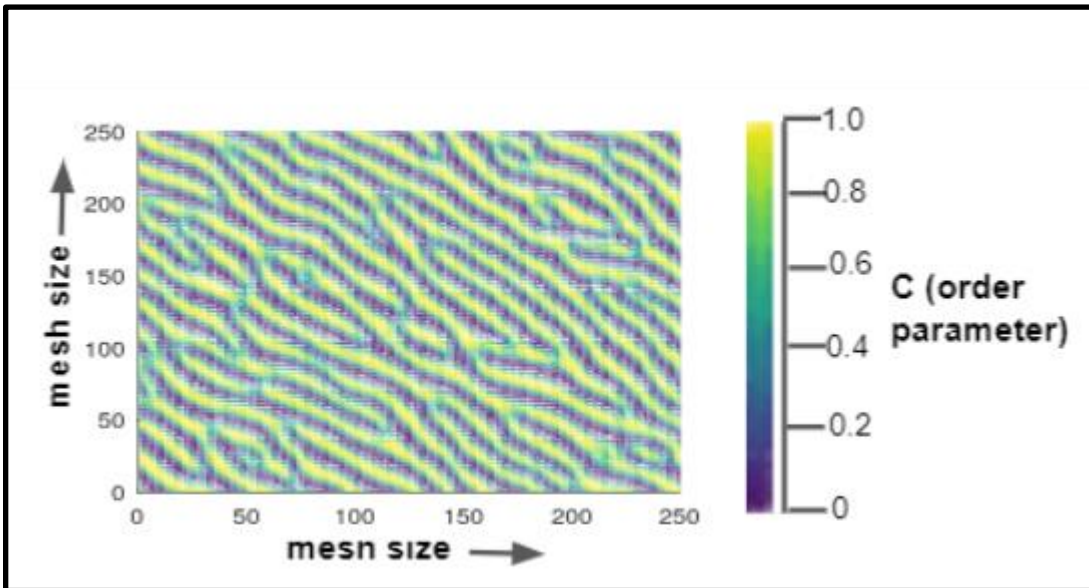


Figure 13(b) Evolved Microstructure for mesh size of 64 x 64

- Large Mesh Size of 250 x 250



**Figure 14(a) Initial Microstructure for mesh size of 250 x 250**



**Figure 14(b) Evolved Microstructure for mesh size of 250 x 250**

Initial microstructure is evolving into regions that are A-rich  $\alpha_1$  phase and B-rich  $\alpha_2$  phase. The random number is different every time and each time we run the simulation we get a different microstructure. Colours tell us what is the value of composition in the plot.

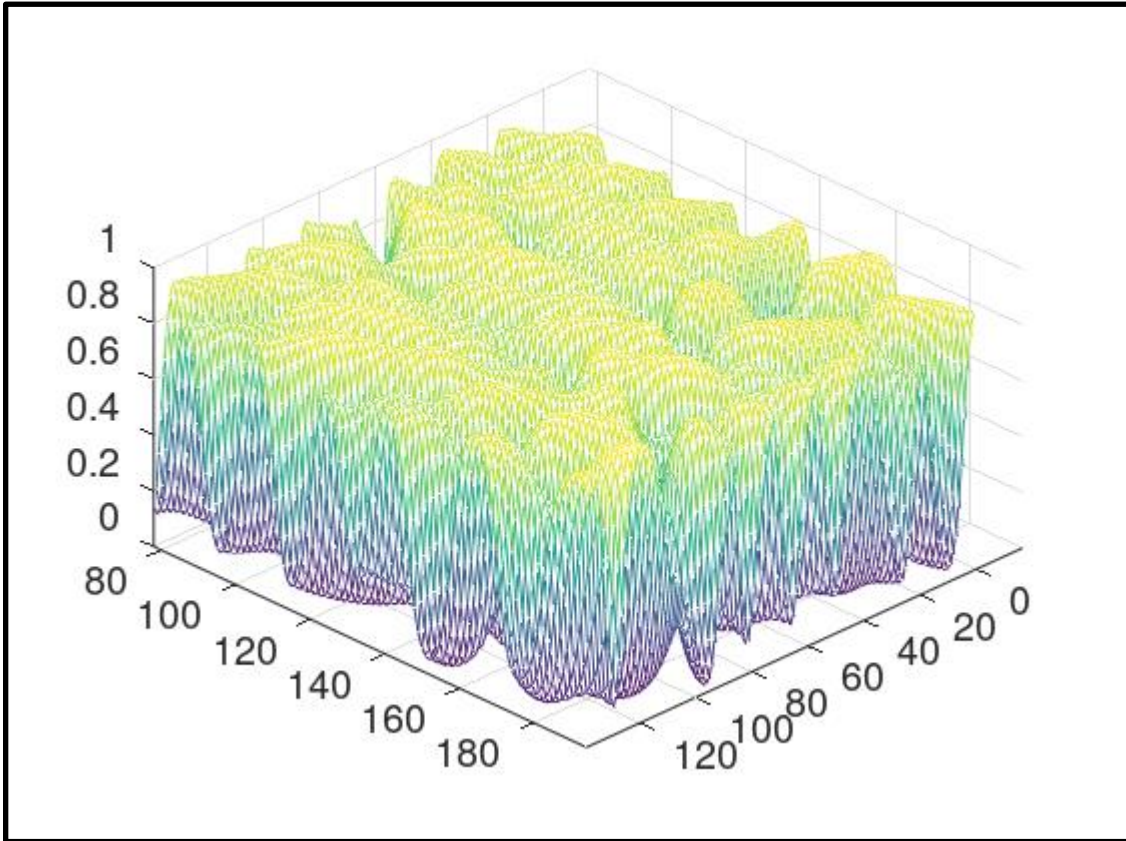


**Figure 15 Evolved microstructure in 3D**

We have obtained the above microstructure simulation using the Cahn-Hilliard equation by plotting in Octave. Above figure 15 shows microstructure evolution in 3D.



## **Chapter 4 - Other applications of Phase Field modelling**

We have used Phase Field modelling for construction of phase diagram and also for plotting spinodal decomposition in a phase separating alloy. Phase Field technique has become an efficient tool for tracking microstructure evolution in phase transformations. It has a broad range of applications. Now in this chapter we will see some existing Phase Field models which are used in some areas of application.

Solidification has long been used as a model for various phase changes that regulate the creation of complex microstructures in materials processing. Solidification is the basis for casting technology and various other processes. For modelling and simulation of microstructure understanding the formations in solidification like dendrite is important. Hence, we will apply Phase Field modelling on solidification. Section 4.1 is about the evolution of microstructure evolution during solidification with electromagnetic stirring. Section 4.2 is about microstructure evolution of Ti-6Al-4V in electron beam additive manufacturing process. Phase Field method is used for tracking grain growth for various conditions. Section 4.3 is about Phase Field model simulation of grain growth in three dimensions under isotropic and anisotropic grain boundary energy conditions. Then section 4.4 explores recent applications of Phase Field models in microstructural evolution for different transformation mechanisms. Some specific applications are discussed in the next two sections. Section 4.5 and 4.6 discuss the application of the Phase Field method in rechargeable batteries and in predicting microstructure, property evolution of irradiated nuclear materials respectively.

In the Phase Field method, Phase Field variables are used. These functions describe the shape and distribution of grains in microstructure. Within grains, the value of Phase Field variables is relatively consistent, but it alters at the interface between two grains. The evolution of Phase Field variables determines the grains' evolution and thus microstructure evolution through some course of duration. In a phase transition system, an order parameter is a measure of the extent of order across the boundaries. The parameters that remain constant with time are called conserved order parameters whereas the ones which do not remain the same are known as non-conserved order parameters. Example of non-conserved quantity is

grains. The total number of grains change over time as microstructure evolves, whereas composition of a material remains the same hence it is a conserved quantity. Modelling of microstructure evolution entails computing order parameters which is triggered by a decrease in the system's total energy.

#### **4.1 Experimental studies and Phase Field modelling of microstructure evolution during solidification with electromagnetic stirring [3]**

Thixocasting needs non-dendritic structure (figure 16) for making billets. In this research paper Aluminium alloy A356 billets are made by Rheocasting technique. Rheocasting is a novel technique for obtaining globular or spheroidal microstructure. Such microstructure has application in automobile engines. In this process the control parameters used are current and duration. Steps involved in the process are discussed for the Aluminium alloy below.

Phase Field model is used to compute solidification morphologies in which Wheeler Model [3] is used.

Binary phase diagram of Aluminium alloy (Al -7Si-0.3 Mg) is shown in figure 17. Some part of this phase diagram is taken in figure 18 to study the heat treatment done to produce the required microstructure with electromagnetic stirring using 250A current and 50 Hz frequency to microstructure shown in figure 19.

From figure 18, Initially alloy is kept at temperature 'a' then it is undercooled by 20 K to 'b' then temperature raised to 'c' and finally undercooled to 'd'.

The various stages in heat treatment and corresponding changes in microstructures are shown in figure 20.

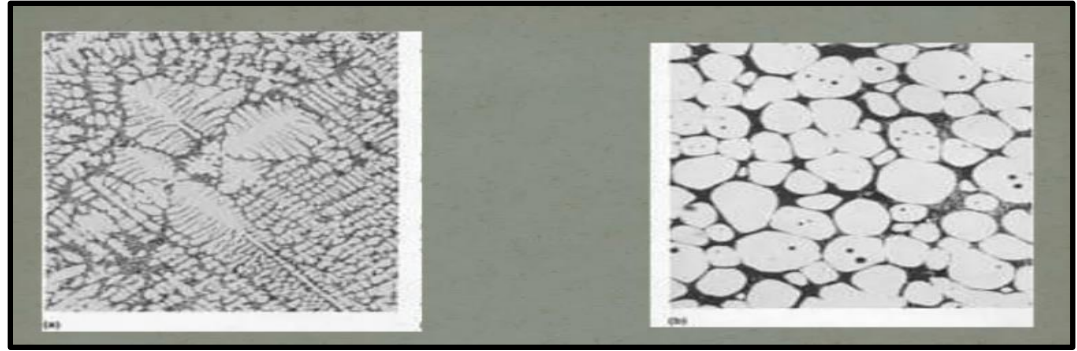


Figure 16 Dendritic Microstructure Non-Dendritic Microstructure [3]

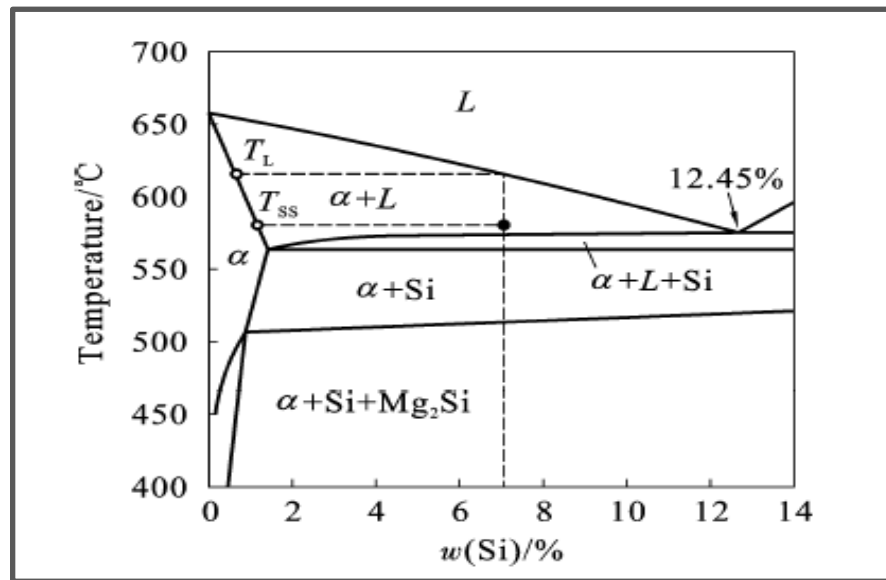
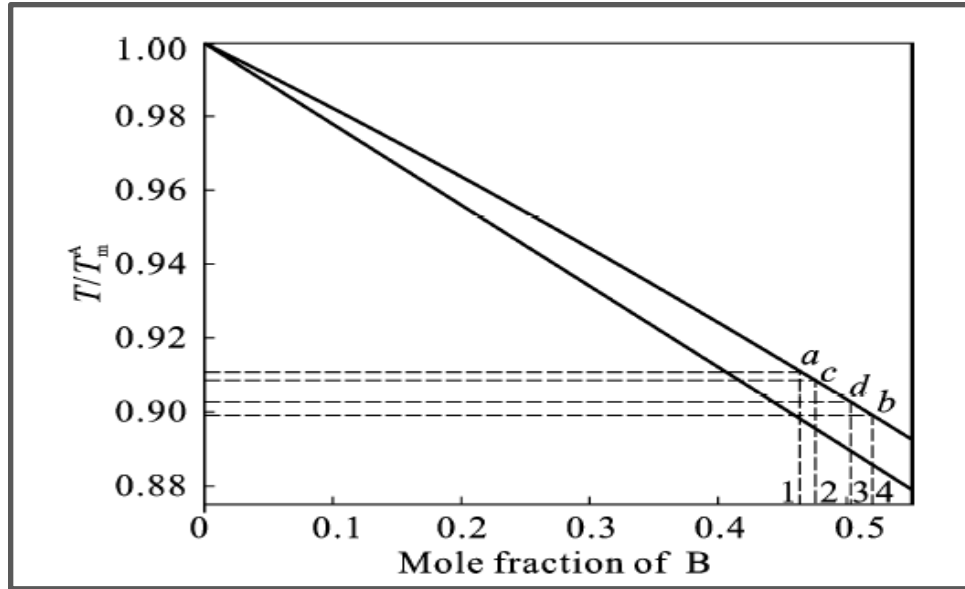
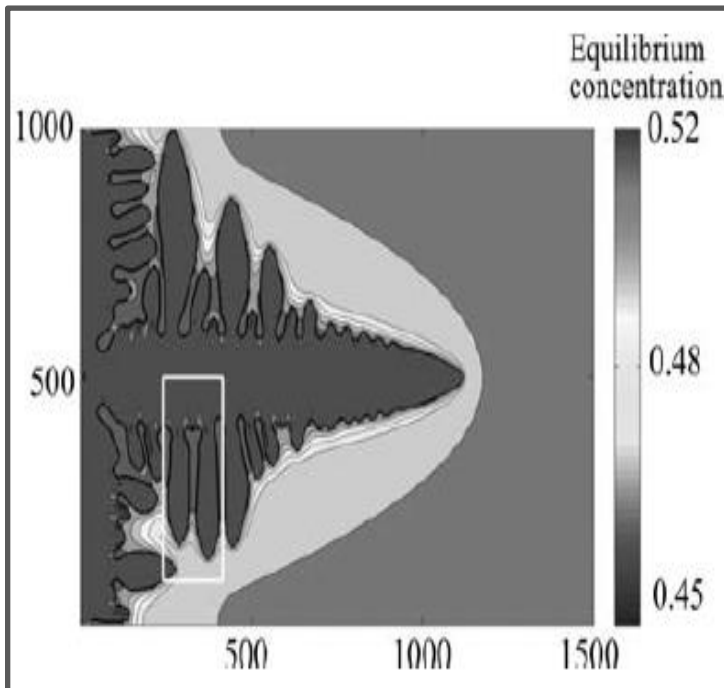


Figure 17 Binary phase diagram of Al-7Si-0.3 Mg alloy [3]



**Figure 18 Simple lens type phase Diagram (Initial at temperature a  $\rightarrow$  b (undercooled to 20K)  $\rightarrow$  c (temperature raised)  $\rightarrow$  d (undercooled)) [3]**



**Figure 19 Dendrite with primary and secondary arms [3]**

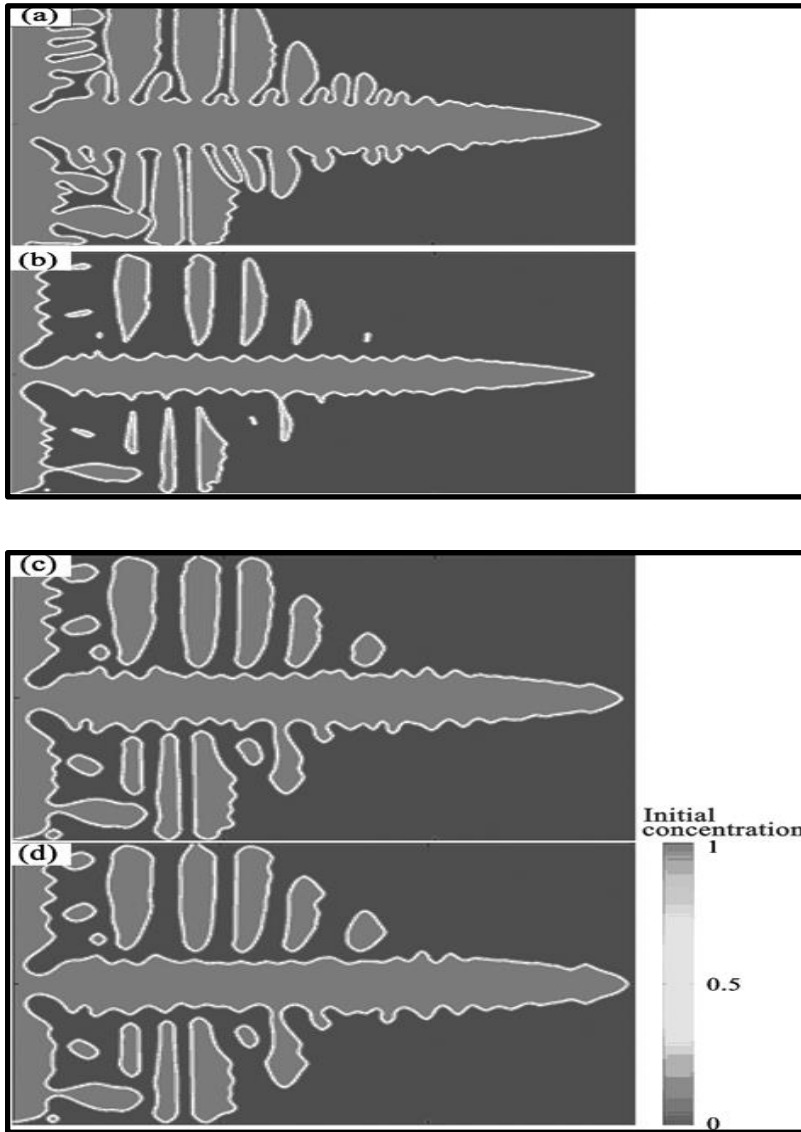


**Figure 20. Phase Field simulation of dendritic to globular transition: (a) Fully developed dendrite; (b) Remelting of dendrite at position c in above Fig.; (c, d) Solidifying at lower temperature at position d (start of globularization) [3]**

## **4.2 Phase Field simulation of microstructure evolution of Ti-6Al-4V in electron beam additive manufacturing process [4]**

Microstructure strongly influences the mechanical properties like tensile strength, ductility, hardness, fracture toughness, creep resistance, etc. But control and optimization of microstructure in real time is a new challenge presently. In this research paper, Ti-6 Al - 4V alloy has been taken for study because this alloy has superior physical and mechanical properties. This alloy has several applications in automobile, aerospace, energy and biomedical.

For producing this high-performance alloy, many additive manufacturing techniques have been used in the last few decades which produce full dense and near net shapes like Electron Beam Melting [4], Laser Melting [4], Selective Laser melting [4], Direct laser Melting [4].

Out of these mentioned techniques, Electron Beam Additive Manufacturing (EBAM) produces metallic components which are solidified layer wise. High energy electron beams melt metallic powders which fuse by rapid self-cooling and produce high density functioning components. EBAM has advantages over conventional techniques like direct fabrication of metallic parts which accelerate product design.

Microstructure evolution is studied by the Phase Field modelling simulation in which two input parameters are given

1. Temperature Gradient
2. Solidification Velocity (Scan Speed)

This simulation is run by using FORTRAN Code.

Effect of temperature gradient and scan speed (electron beam speed) on microstructure is studied via simulations.

### **Effect of Temperature Gradient on Microstructure**

The figure 21 shows how different temperature gradients affect the microstructure during solidification. With increase in temperature gradient from figure 21(a), figure 21(b), figure 21(c) to figure 21(d), we can observe the microstructure is becoming finer and columnar microstructure is obtained.

The above discussion is validated by studying variation of dendritic spacing and width of dendritic arms with temperature gradient shown in figure 22 and figure 23 respectively.

Figure 22 and 23 indicate that dendritic spacing and width of dendritic arms decreases with increase in temperature gradient which indicates that microstructure is becoming finer and columnar microstructure is obtained.

### **Effect of different Scan Speed on Microstructure**

The figure 24 shows how different scan speeds affect the microstructure during solidification. With increase in scan speed from figure 24(a), figure 24(b), figure 24(c), figure 24(d) to figure 24(e) we can observe the microstructure is becoming finer and columnar microstructure is obtained.

The above discussion is validated by studying variation of dendritic spacing and width of dendritic arms with scan speed shown in figure 25(a) and figure 25(b) respectively.

Figure 25(a) and 25(b) indicate that dendritic spacing and width of dendritic arms decreases with increase in scan speed which indicates that microstructure is becoming finer and columnar microstructure is obtained.

### **Validating the Phase Field simulation**

Powders of Ti, Al and V are taken in the ratio of 90: 6: 4 and mixed. Beam speed is used for solidification of this alloy is 400 mm/s. Small piece of sample is taken which is mounted on epoxy and metallographic observation is done by doing fine polishing.

When a sample is observed under the Scanning Electron Microscope (SEM) and compared with simulated microstructure (figure 26), columnar dendrites are observed.

Finally, simulated and analytical microstructure are compared in terms of columnar dendritic spacing (figure 27), it is found that both matches approximately. Thus, this validates

the Phase Field simulation with analytical microstructure.

A theoretical model (Hunt's Model) is developed to explain the differences in dendritic tip temperatures with velocity and temperature gradient.

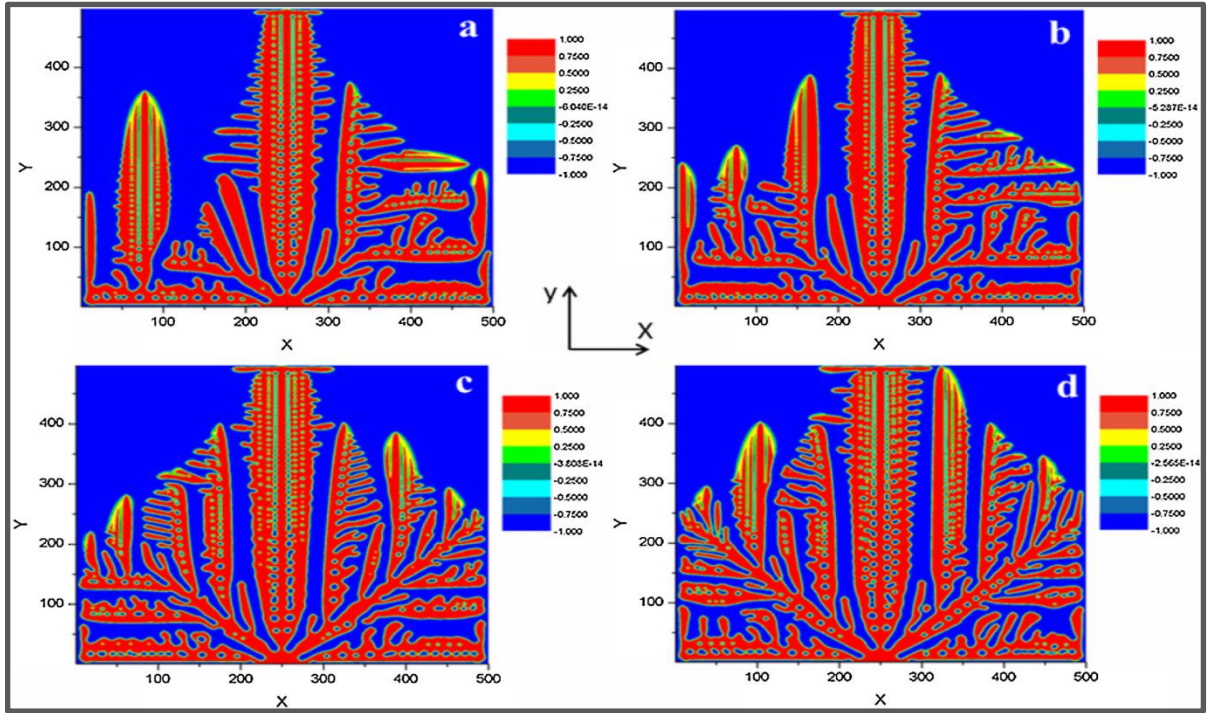


**Figure 21** Phase profile of Ti-6Al-4V at different temperature gradient (a) 2222.72°C mm<sup>-1</sup>, (b) 2294.13°C mm<sup>-1</sup>, (c) 2506.12°C mm<sup>-1</sup> and (d) 2822.77°C mm<sup>-1</sup>. [4]

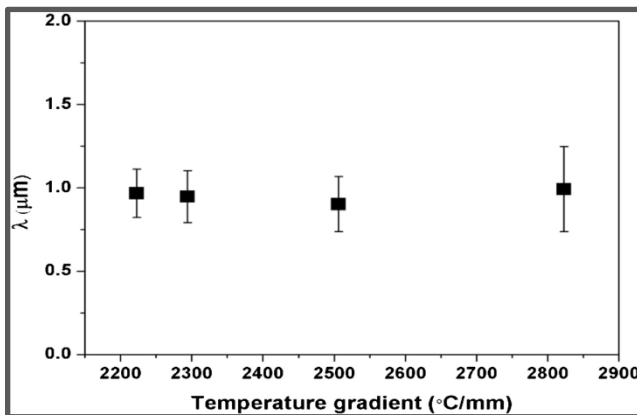


**Figure 22** Variation of columnar dendritic spacing with temperature gradient. [4]



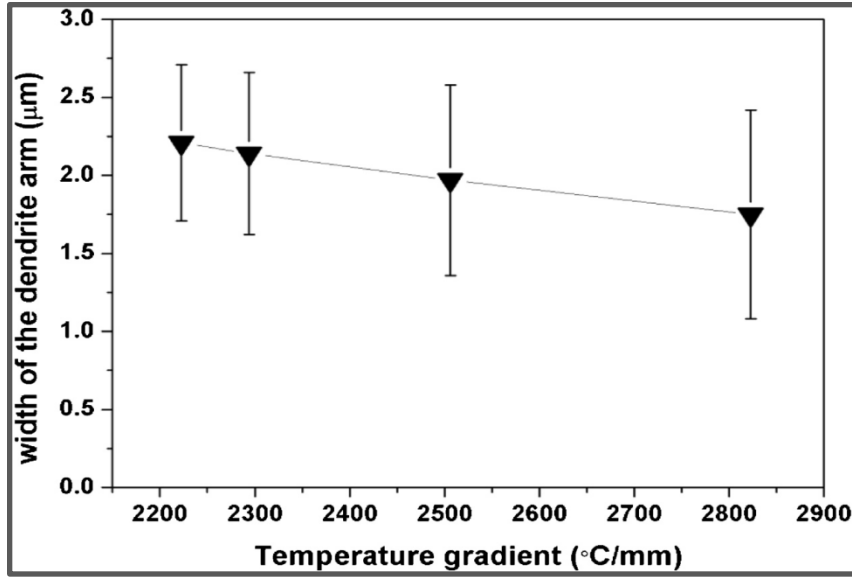


Figure 23 Variation of width of dendritic arm with temperature gradient. [4]

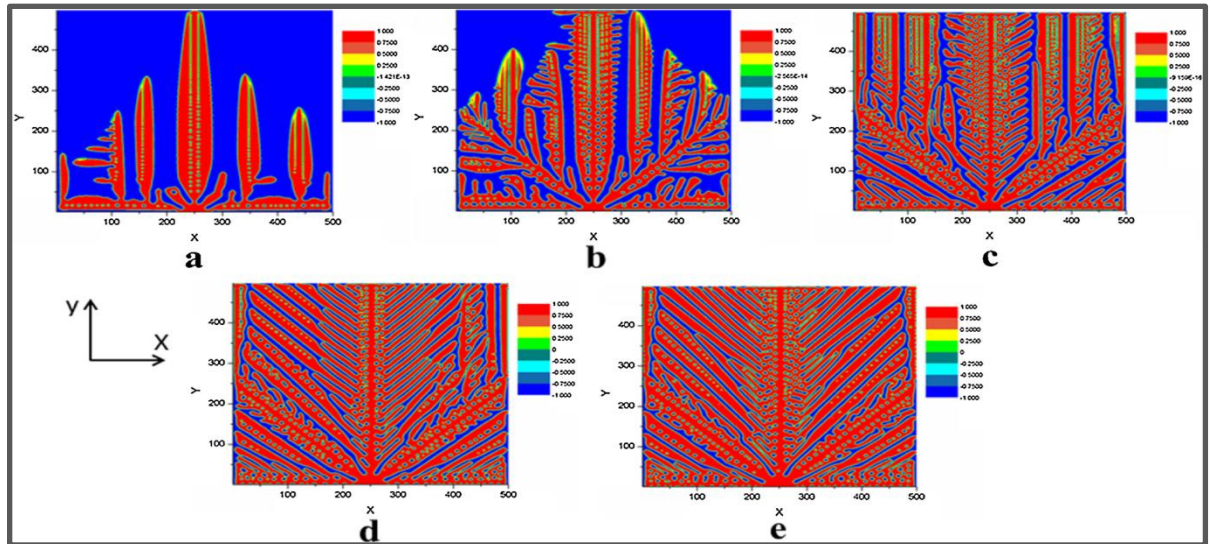


Figure 24 Phase profile at different scan speed (a) 200 mm s<sup>-1</sup>(b) 400 mm s<sup>-1</sup>(c) 600 mm s<sup>-1</sup>(d) 800 mm s<sup>-1</sup>(e) 1000 mm s<sup>-1</sup> [4]

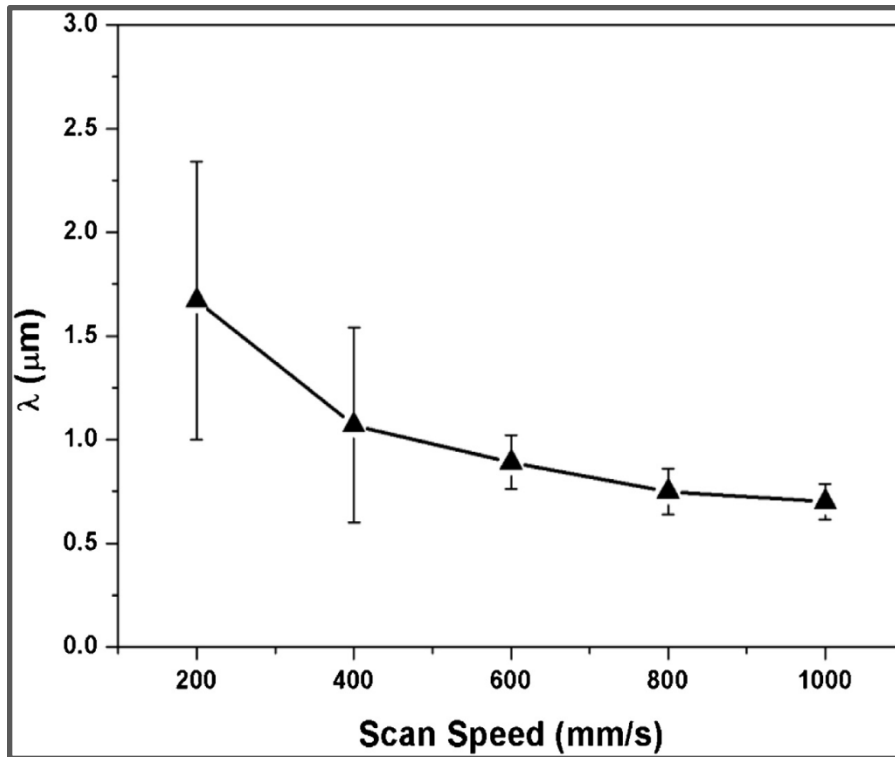


Figure 25(a) Columnar dendritic spacing with scan speed. [4]

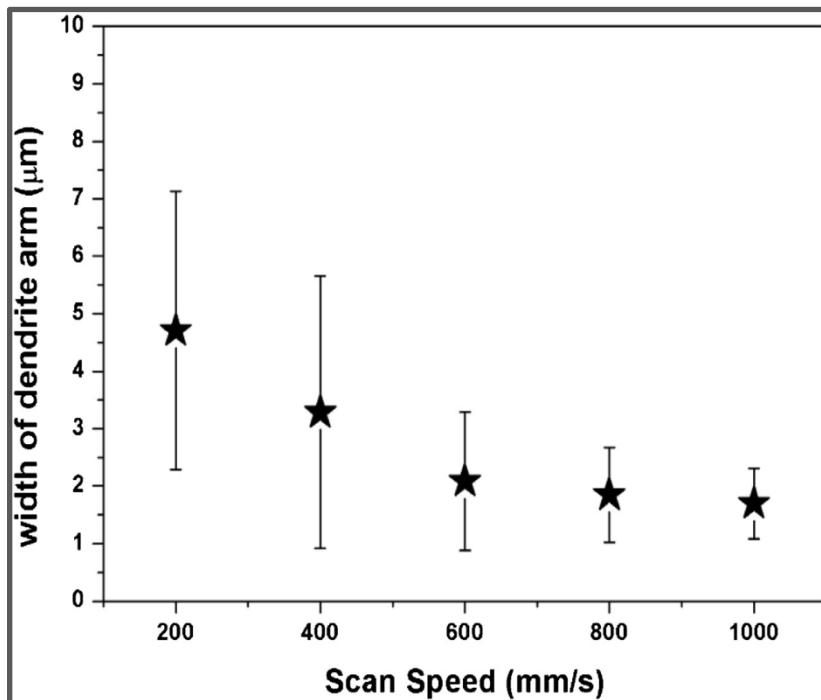
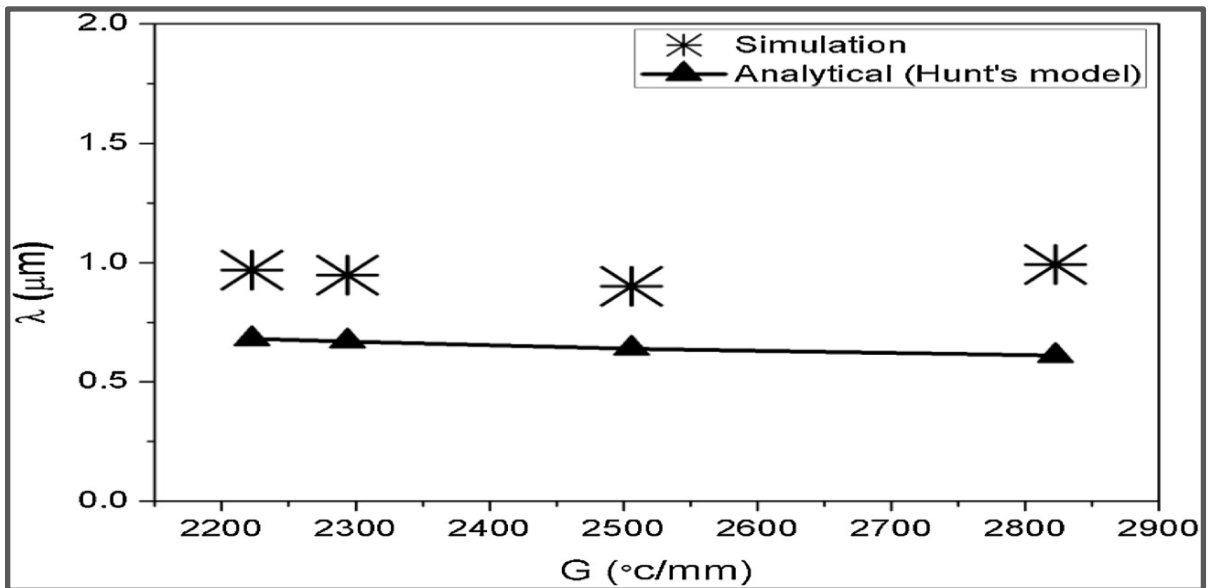
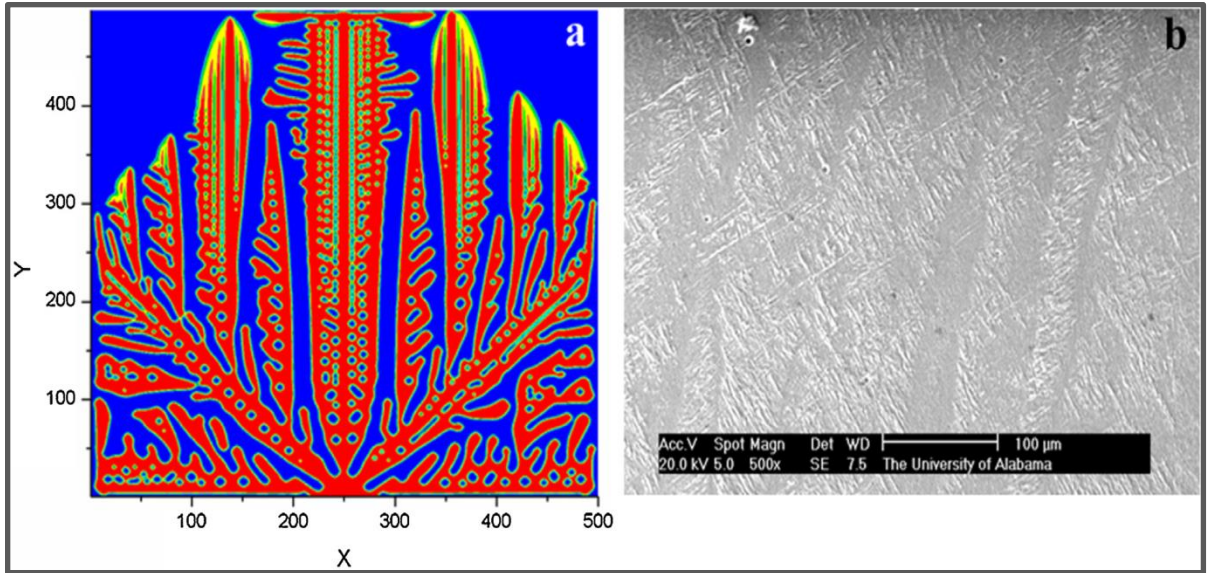


Figure 25(b) Width of dendrite arms with scan speed. [4]



### **4.3 Phase Field model simulation of grain growth in three dimensions under isotropic and anisotropic grain boundary energy conditions [5]**

The decrease in the entire grain boundary area drives grain growth. For grain growth, its size is a key parameter. In isotropic grain boundary energy, where larger grains expand while smaller grains contract. However, for anisotropic grain boundary energy, grain boundary energy has a significant influence in grain growth. Grains with low grain border energy expand more readily, while the grains with high grain boundary energy contract more readily.

The microstructure evolution of three-dimensional grain growth was simulated using the Phase Field method in this research under both isotropic and anisotropic grain boundary energy conditions. A series of non-conserved order parameters, representing grain orientations, were used to define the microstructure in the simulation.

#### **Simulation of grain growth for isotropic grain boundary energy**

For a grain growth model, a primary microstructure that approximates the actual scenario should be built. Randomly oriented grains were strewn across the simulation model, which were then allowed to grow for some duration. The system after thousand iterations is illustrated in figure 28(a), which is considered as the initial microstructure for this simulation. Grain borders and grains are depicted by the white and black patches, accordingly. Figures 28(b) and 28(c) illustrate a two-dimensional portion of the microstructures after two thousand and four thousand iterations, indicating normal grain development. After thousand iterations, the distribution of grain did not alter over the course of the experiment and had reached a steady state of grain growth. For distinct simulation durations of thousand, two thousand, three thousand four thousand and five thousand. Figure 29 displays distribution of grain size standardised by the mean size. Figure 30 depicts how the mean grain size has changed with the duration of simulation.

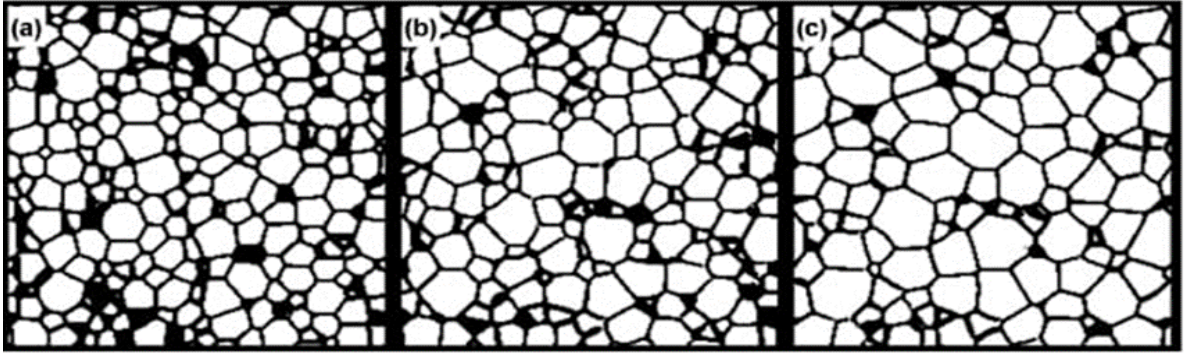


Figure 28 2D sections of microstructures after (a) 1000, (b) 2000, (c) 4000 iterations. [5]

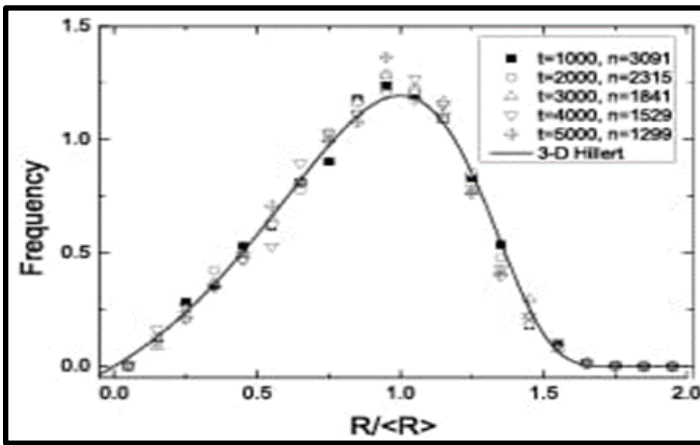


Figure 29. Grain size distribution data [5]

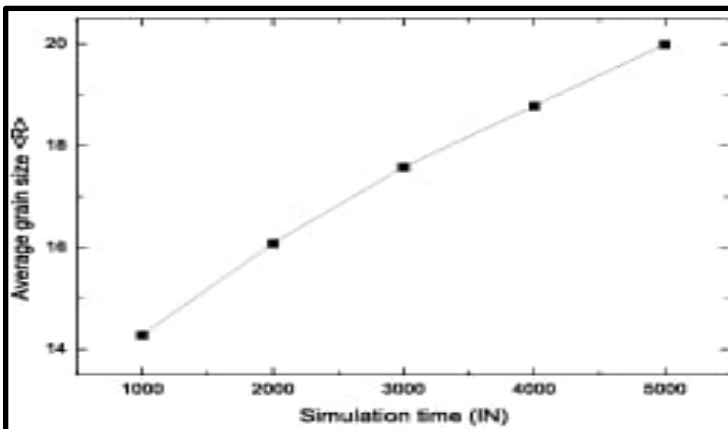
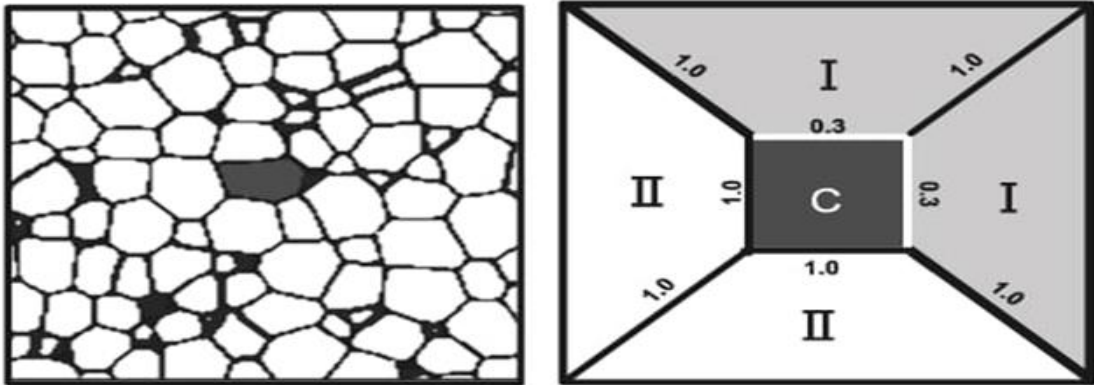


Figure 30 Time evolution of the average grain size [5]

### Simulation of grain growth for anisotropic grain boundary energy



**Figure 31 (a) 2D section of initial microstructure of simulation. (b) grain boundary energies to each kind of boundaries [5]**

A two-dimensional slice of the starting microstructure is shown in figure 31(a). The type C grain in the centre of figure 31(a) was classified, while the remaining grains are classified into type I and II. The grain boundary energy assigned to each type of grain boundary is shown in figure 31(b). Grain boundary energy of the C grain is low i.e. zero point three with type I grains. And it is high, i.e. one with type II grains. Those among I and I, II and II, and I and II are examples of grain boundaries with high energy of one. In this system, type I grains accounted for thirty percent of the entire system, while the type II grains accounted for seventy percent. Thirty percent of the boundaries of the C grain have a low energy of zero point three in this situation. This provides the C grain an edge for growing. C grain has a chance of growing due to solid-state wetting.

If the anisotropic grain boundary energy meets the wetting condition at the triple junction, i.e. one grain boundary's energy is greater than the sum of the other two grain boundaries' energies, then the high energy grain boundary will be replaced by the two lesser energy grain boundaries. At the triple junction point, where the C grain comes into contact with the two type I grains, grain boundary wetting occurs. At the quadruple junction, in which the type C grain is in contact with two or three type I grains, triple junction wetting can occur.



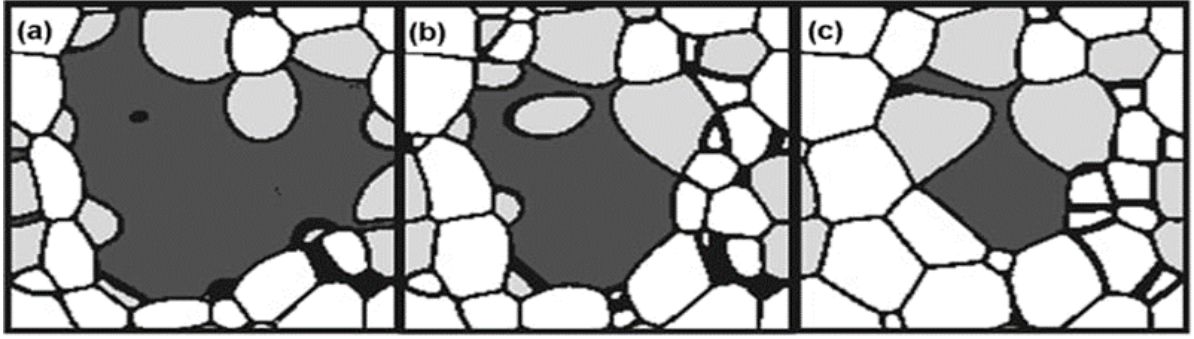


**Figure 32** 2D section of microstructure evolution after 4000 iterations with decreasing percentages of type I grains. [5]

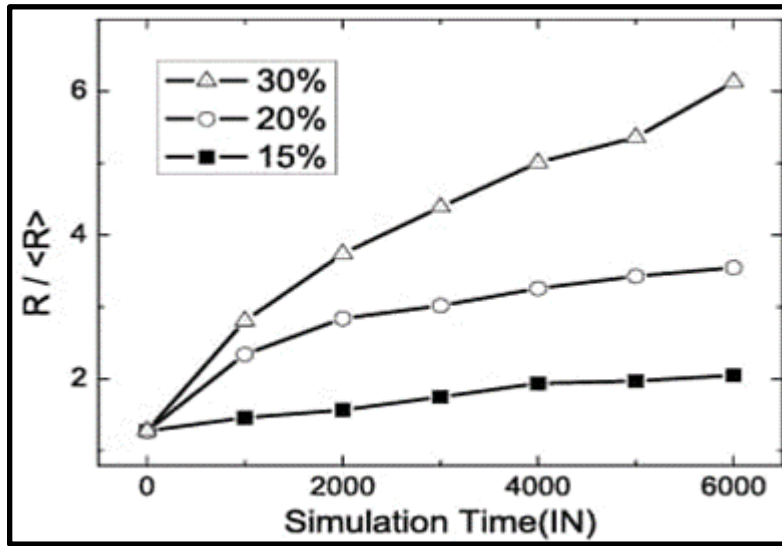


**Figure 33** Time evolution of average grain size [5]

The chance of wetting by the type C grain falls as the percentage of I grains decreases, as seen in figure 32. As a result, the dark type C grain's growth rate is decreased. Wetting causes the island and peninsular grains to develop. For varying percentages of type I grains, the size of C grain standardised by the mean size, is presented against duration of experiment in figure 33.  $R / \langle R \rangle$  grows with a simulation period in all three scenarios and all the curves have positive slope, implying abnormal grain development.

The microstructure developed by simulation exhibits typical grain development when the grain boundary energy is isotropic. The grain with a low energy grain border could grow

via solid-state wetting in the presence of anisotropic grain boundary energy. The grain grew abnormally when the wetting probability was high enough.

#### **4.4 Phase Field modelling of microstructure evolution: Recent applications, perspectives and challenges [6]**

The processing-microstructure-properties relation is important since the phases at the microscopic level have a significant role on the macroscopic behaviour of materials. This creates the necessity to study the numerical simulations at the mesoscale for comprehending the processing-structure-properties interactions by which a material can be designed with required properties. The finite element approach has been used to link microstructure to properties. In this the region is segmented into homogeneous areas separated by boundaries, and each zone's reaction is regulated with partial differential equations. The Phase Field approach has been established as a valuable method for modelling the evolution of microstructures.

Various solid-state transformations of microstructural evolution have been studied using the Phase Field approach. Recent research of mechanisms, including diffusive transformation (precipitation) [6], displacive transformation (martensite) [6], and deformation mechanism (twinning) [6], are highlighted in this study.

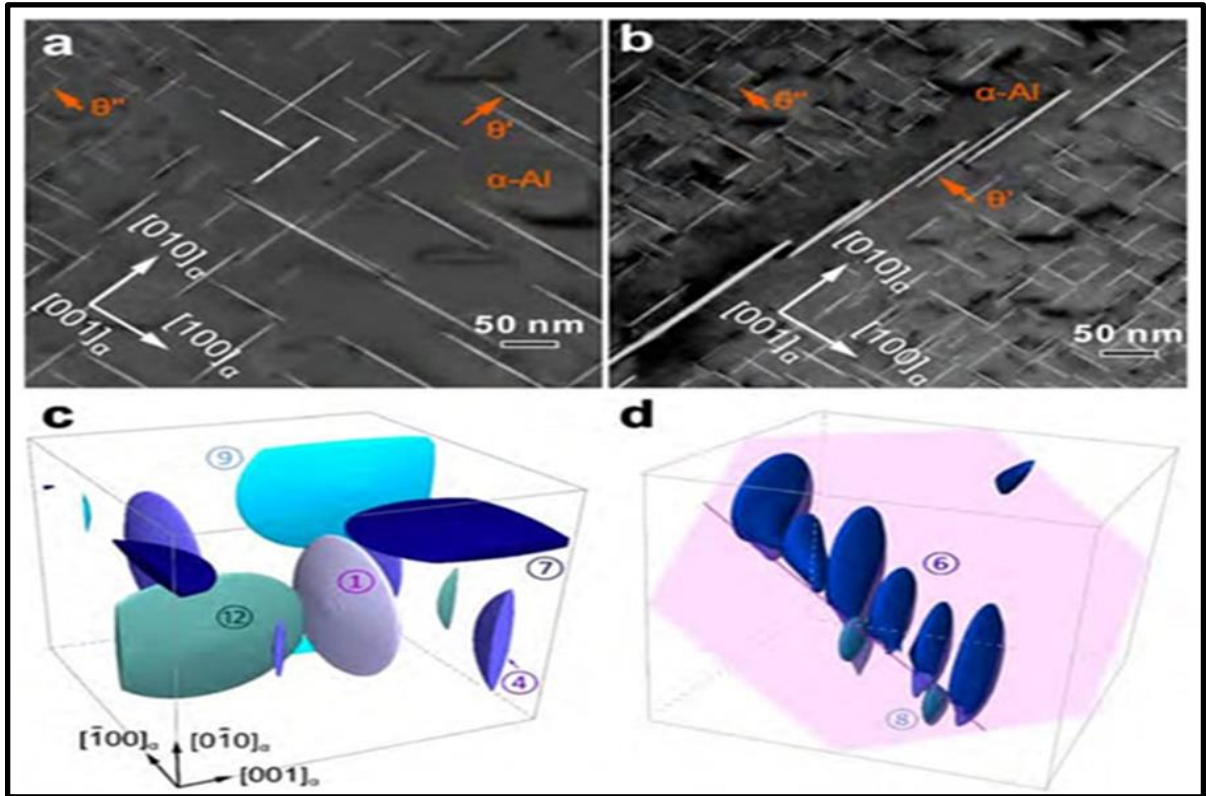
##### **Precipitation**

To analyse precipitation in metallic alloys, the Phase Field approach has been extensively used. Studies and research have looked into the structure and distribution of precipitates. It has also explored the interactions between precipitates and stress fields induced by other precipitates or lattice defects.

In Al-Cu alloys, the Phase Field approach is used to investigate the formation of precipitation  $\theta'$ . In these alloys, the  $\theta'$  is a critical strengthening phase. Input factors such as transformation strains, elastic constants, free energy curves of both  $\theta'$  precipitates and matrix,



and interfacial energy between  $\theta'$  precipitates and matrix are needed to effectively estimate the shape and process of forming of  $\theta'$  precipitates. These factors can be determined using numerical methods, or data from already existing sources. The interfacial energy and elastic strain energy both favour precipitate growth along the same habit plane, and shear strain dominates the shape of  $\theta'$ , as per simulation studies. Pre-existing lattice defects, like dislocations, have been demonstrated to aid the nucleation and growth of precipitates in alloys.



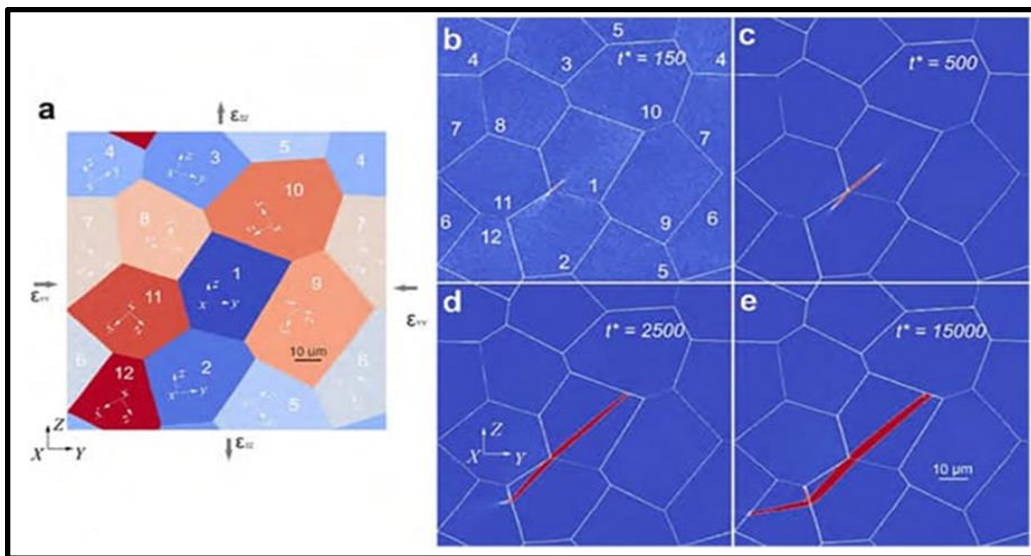
**Figure 34 TEM image and simulated image of precipitates in Al-Cu alloy [6]**

Figure 34(a) and (b) are TEM images of  $\theta'$  precipitates in an Al-Cu alloy. Figure 34(a) is of random precipitation of  $\theta'$ . Figure 34(b) shows orientation-correlated precipitation of  $\theta'$  in the alloy. Figure 34(c) is a Simulation of homogeneous nucleation of  $\theta'$  precipitates using Phase Field. This results in randomly distributed precipitates, while figure 34(d) represents the  $\theta'$  phase produced in a mixed dislocation stress field, resulting in correlated orientations.

The contrast in the TEM image is related to the atomic number. Copper content is higher in phase  $\theta'$  than in the matrix. Hence  $\theta'$  precipitates appear brighter than matrix. As a result, the dispersion of  $\theta'$  precipitates were shown using TEM micrographs.

### Deformation Twinning

Twinning is a deformation mechanism. It has been examined with the Phase Field approach. The generation and nucleation of twins in a polycrystalline Magnesium microstructure was examined by utilising Phase Field technique, as shown in figure 35. The applied strain triggers the nucleation of twin crystals at the triple junction point. It grows and promotes the formation of further twin crystals in nearby grains. This eventually results in formation of a twin chain that thickens until a steady state structure is obtained.



**Figure 35 Twinning in Magnesium [6]**

### Martensitic transformation

The fast transformation kinetics of martensite formation makes observing in situ difficult. This makes the modelling and simulations even more valuable. Figure 36, illustrates an implementation of the Phase Field approach to the martensitic transformation. Observed microstructures in low-carbon steels are analysed with the modelled microstructures in this

study. The figure shows martensite microstructure considering twenty-four orientation variants. The shades of one colour represent variants with the same Bain deformation.

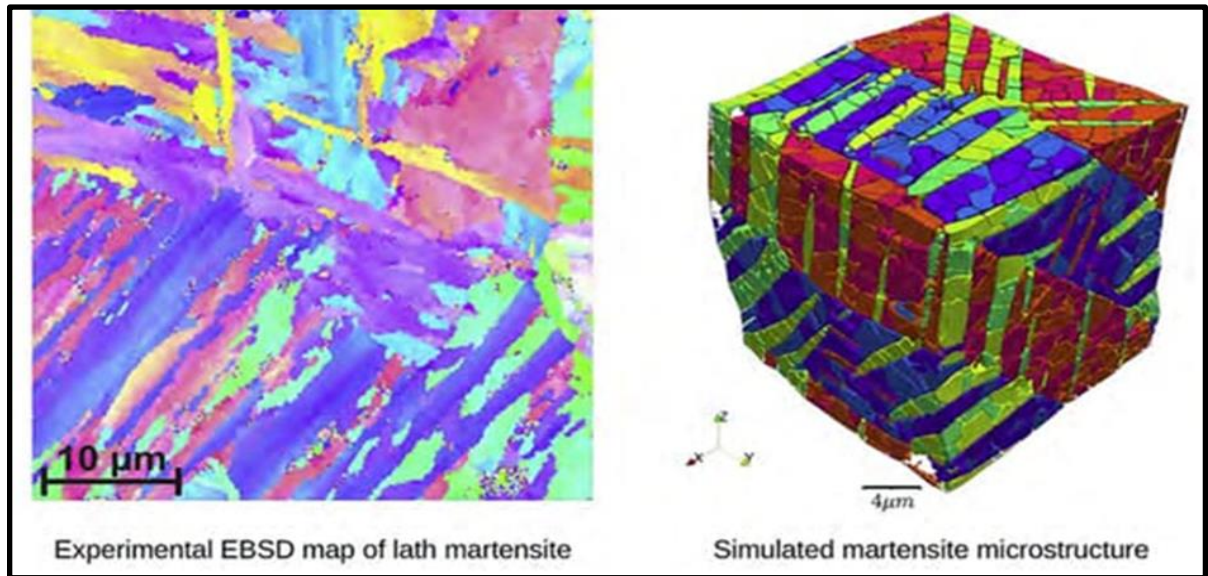


**Figure 36 Experimental and simulated martensite [6]**

Quantitative microstructure evolution estimates entail in accurately identifying the variables and relationships. This can be done from experiments as well as from the simulation methods. The computational cost of the Phase Field approach is a significant constraint, limiting the length and time scales of application. Numerical approaches help in overcoming this limitation to some extent. In addition, machine learning can be utilised to quickly solve partial differential equations. As Phase Field modelling has become a standard computational engineering method, the production of standard benchmark issues has become an important situation.

## **4.5 Application of the Phase Field Method in rechargeable batteries [7]**

Rechargeable batteries significantly affect our day-to-day existence with the goal of capturing the chemical and physical basics influencing the activity and lifespan. Phase Field method is a strong computational way to deal with portraying and anticipating the development of microstructures of mesoscale, which can assist with getting the unique way of behaving of the material frameworks. In this survey, Present the theoretical framework of the Phase Field model. Its application in electrochemical systems, summarise the current Phase Field simulations in RBs (rechargeable batteries), and give advancement, and issues to be considered of things to come in Phase Field simulation in RBs (rechargeable batteries). During the previous many years, the examination of electrochemical energy capacity has grown quickly, particularly in rechargeable batteries (RBs), which have been completed.

### **Modelling in Rechargeable Batteries**

In thermodynamics, a spatial region with a moderately uniform and stable structure is characterised as phase, and a field is a component of space and period of time. In a real sense, the Phase Field model is a computational model which depicts the microstructure advancement of material frameworks as an element of space and time. One element of the Phase Field model is the diffuse interface.

The Phase Field model describes the phase states of systems by using Phase Field variables ( $a= 1,2,...,n$ ).

$$\frac{\partial \phi_a}{\partial t} = - \sum_{\beta} L_{a\beta} \frac{\delta f}{\delta \phi_{\beta}}. \quad \dots \text{eq. 4.1}$$

Not only one component in the system; so concentration variables  $c_i$  ( $i=1; 2, \dots, n$ );  $m$  should be introduced to describe the system

$$\frac{\partial c_i}{\partial t} = \nabla \cdot \left( \sum_j M_{ij} \nabla \frac{\delta f}{\delta c_j} \right). \quad \dots \text{eq. 4.2}$$

For solving Equations 4.1 & 4.2, the total free energy of the system (which include chemical energy, mechanical energy, etc.) should be expressed as a function of the introduced field variables:

$$F = \int_V f dV = \int_V (f^{\text{chem}} + f^{\text{elec}} + f^{\text{elas}} + \dots) dV. \quad \dots \text{eq. 4.3}$$

### Electrochemical Phase Field model

Electrochemical systems involve electric fields and sometimes elasticity, and the Phase Field model can be applied to them.  $f^{\text{elec}}$  and  $f^{\text{elas}}$  can be expressed as follows:

$$f^{\text{elec}} = \rho^{\text{elec}} \Phi = \sum_{i=1}^m \frac{F_0 z_i \Phi}{V_{\text{mol}}},$$

$$f^{\text{elas}} = \sum_{\alpha=1}^N \frac{1}{2} h(\phi_\alpha) (\boldsymbol{\varepsilon}_\alpha - \boldsymbol{\varepsilon}_\alpha^0) : \mathbf{C}_\alpha : (\boldsymbol{\varepsilon}_\alpha - \boldsymbol{\varepsilon}_\alpha^0). \quad \dots \text{eq. 4.4}$$

$\rho^{\text{elec}}$  denotes the charge density,  $F_0$  denotes the Faraday constant (scalar),  $z_i$  denotes the valence of the component  $i$ ,  $V_{\text{mol}}$  represents the volume of the system,  $\boldsymbol{\varepsilon}_\alpha$  and  $\boldsymbol{\varepsilon}_\alpha^0$  denote the eigen strains of phase  $\alpha$ , and  $\mathbf{C}_\alpha$  denotes the stiffness of phase  $\alpha$ .

The equations of strain and electric potential are as follows:

$$\frac{\partial \rho^{\text{elec}}}{\partial t} = \nabla \cdot (\boldsymbol{\sigma}^{\text{elec}} \nabla \Phi),$$

$$\nabla \cdot [\mathbf{C}_\alpha : (\boldsymbol{\varepsilon}_\alpha - \boldsymbol{\varepsilon}_\alpha^0)] = 0. \quad \dots \text{eq. 4.5}$$

The modified Phase Field and concentration equations can be expressed as

...eq. 4.6

$$\frac{\partial \phi_a}{\partial t} = - \sum_{\beta} L_{a\beta} \frac{\delta f}{\delta \phi_{\beta}} + V_{\text{mol}} \sum_i n_{i,a},$$

$$\frac{\partial c_i}{\partial t} = \nabla \cdot \left( \sum_j M_{ij} \nabla \frac{\delta f}{\delta c_j} \right) + V_{\text{mol}} \sum_a n_{i,a}.$$

### **Ionic diffusion**

Researchers used a continuum Phase Field model that incorporated anisotropic (orthorhombic) and inhomogeneous elastic impacts to simulate diffusion-restricted phase changes during Li intercalation in LiFePO<sub>4</sub> nanoparticles. Multiscale models that coordinate DFT estimation and Phase Field simulation are promising ways to extend the safety and long-term circulation capabilities of solid-state batteries. The effective ion conductivity of  $\beta$ -Li<sub>3</sub>PS<sub>4</sub> electrolyte was anticipated through the Phase Field simulation They found a sulphide Li<sub>3</sub>AlS<sub>3</sub>, which grows the opportunities for investigating new fascinating structures by means of Phase Field simulations.

### **Stress evolution and fracture**

Anode Phase Field models have traditionally treated lithiation stress as diffusion-induced pressure, i.e. Li diffusion causes the composition to deviate from its stoichiometric state during anode lithiation. In the case of non-uniform Li distribution, a deviation from



stoichiometry for the most part produces pressure and is a promising cutting-edge anode material for Li-particle batteries due to the minimal expense and high theoretical limit. The lithiation and de-lithiation of the Si anode cause elastic and plastic deformation. A Phase Field model combined with enormous elastic-plastic deformation to explore the phase development, morphology, and stress alleviation inside the crystalline Stress produced by diffusion by means of development and shrinkage in intercalation and de-intercalation of metal cations causes micro cracks, which leads to fracture with large deformation. To understand the structural stability of a battery electrode, it is crucial to understand how cracks propagate in the electrode during charging-discharging.

Figure37 Crack propagation during DE lithiation process. (a) an Initial state, (b) phase segregation, (c) phase interface and crack tip movement, (d) crack tip begins to branch, (e) phase interface moves towards the centre, (f) final state

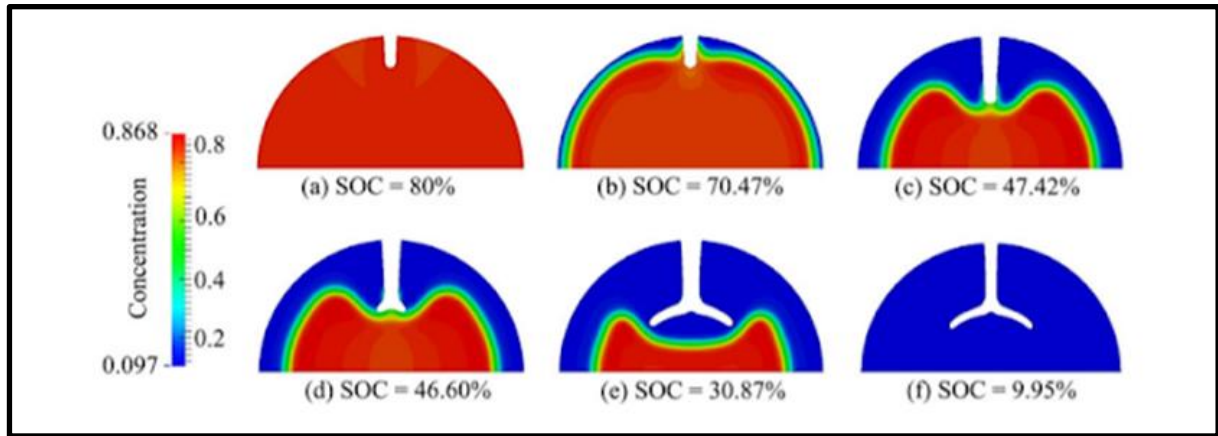


**Figure 37 Crack propagation during the de-lithiation process. [8]**

### **Electrodeposition and dendrite growth**

Li-particle RB's and arrangement of Li dendrite during charging processes are one of the fundamental obstructions in their broad application, which will bring about a decline in reversible limit and an internal short circuit crystalline. Upon Li, deposition of the outer layer of the anode particles generally cracks because of volumetric extension, and new Li is uncovered for additional responses Li dissolution in discharging processes makes pits and

crevices with low impedance and Li-particle stream at the deformities prompts fast development of metal filaments and dendrites. Thus, understanding the actual systems of this complex non-equilibrium process is fundamental to work on the presentation of Li-particle batteries. Liang and Chen [9] introduced by Taking into account Butler-Volmer kinetics, this nonlinear Phase Field model can predict the Li deposit development during charging processes disregarding the SEI layer effect.

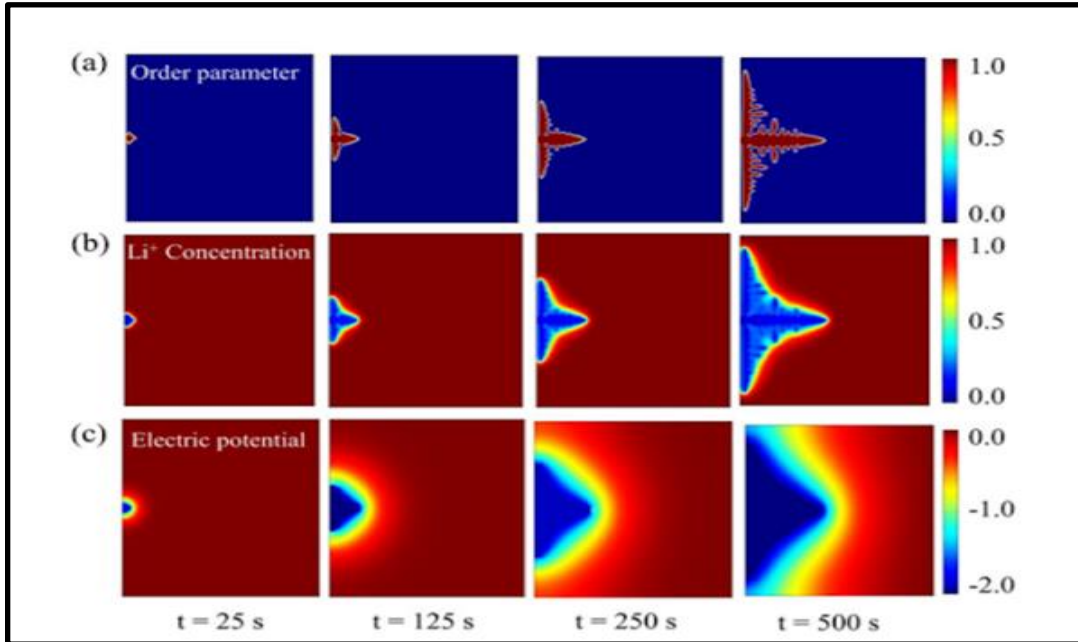


**Figure .38 Phase Field simulations of Li dendrite growth. Evolution of an order parameter, b Li+ concentration, c electric potential. [9]**

There are three levels of Phase Field simulation:

- The first level portrays a material's microstructure development and looks at microstructure progress of comparative materials.
- The subsequent level breaks down the connection between microstructure and execution and predicts the presentation development of the framework as per its simulation results.



- The third level works on the presentation of the framework in light of its impact factors and controls its better help execution by changing its physical environment.

Phase Field simulations in rechargeable batteries (RBs) have a place with the first two levels; explicitly, the majority of simulations are still in the primary level. Progress of Phase Field simulations for RBs toward quantification needs precise thermodynamic and dynamic data sets of the framework disregarding the SEI layer effect.

#### **4.6 Applications of the Phase Field method in predicting microstructure and property evolution of irradiated nuclear materials [10]**

Because of the extreme conditions of serious irradiation and high temperature, nuclear fuel and structural materials undergo complex microstructural changes. This paper examines the role of the Phase Field technique in anticipating microstructural evolutions and their effects on mechanical, thermal, and magnetic properties of these materials. This begins with an outline of the significant actual systems of imperfection evolution and the critical holes in microstructure evolution in irradiated nuclear materials.

Nuclear fuels and primary parts of nuclear reactors can undergo drastic changes in their morphology and thermo-mechanical properties when exposed to high-energy particles (such as neutrons, ions, and electrons) as a result of radiation-induced evolution of compositions and microstructures. The fundamental impacts of radiation on the reactor, materials are (1) gas bubble enlarging associated with dimensional change, void expanding, grain growth, and creep; 2) increase in ductile-brittle transition temperature (DBTT) and loss of ductility because the formation of the second phase precipitates, self-interstitial atomic (SIA) circles, and dislocation networks (3) corrosion and oxidation speed up by ultimate high temperature, fission items, and radiation harm. Figure 39&40 shows normal microstructures noticed in irradiated materials

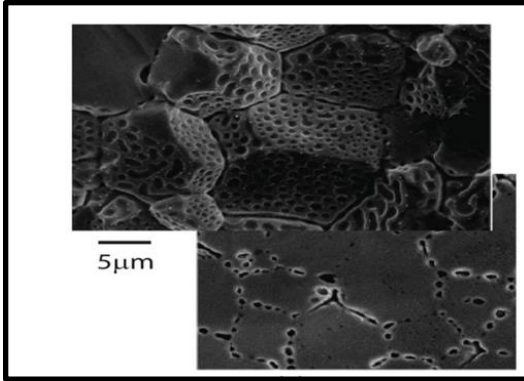


**Figure 39** Scanning electron microscope (SEM) image of gas bubble structure in UO<sub>2</sub> [11]

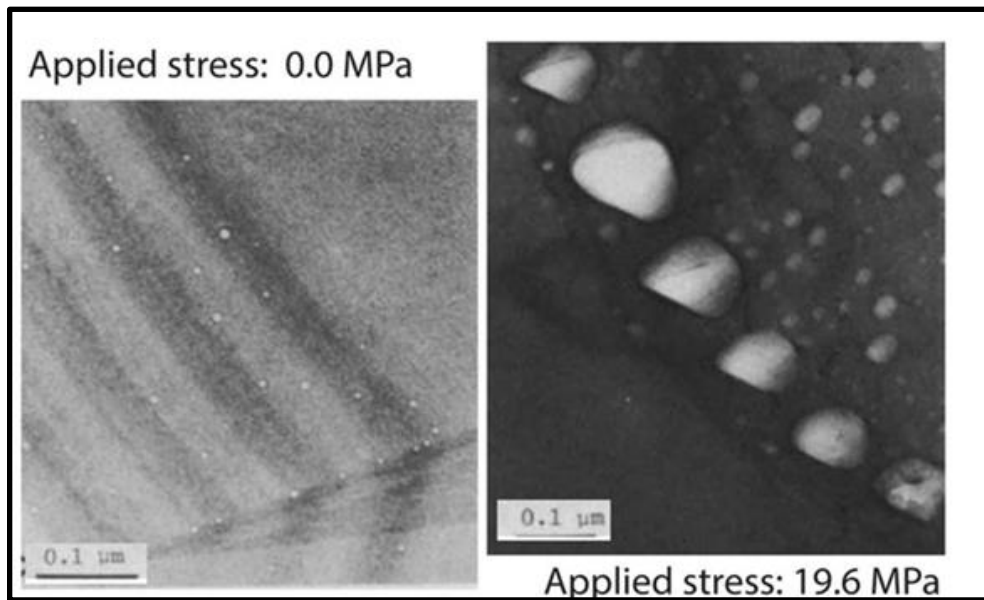


**Figure 40** Effect of tensile stress on helium gas bubble structure in Fe-17wt% Cr-17wt% Ni after annealing at 1023 K for 60 h [11]

### **Irradiation effects on mechanical, thermal, and magnetic properties**

Phase Field techniques have been successful in anticipating the impact of microstructure and chemistry on the mechanical properties of materials. However, PF methods are not immediately applicable to predicting the impact of radiation-induced microstructures on mechanical properties. The Phase Field method that took the understanding

of and prediction of gas bubble expansion, which affected the thermomechanical properties of irradiated materials, to the next level with regards to irradiated materials, During the activity of nuclear reactors, void space and additionally gas bubbles enlarge significantly. This is observed in both nuclear fuel and cladding materials.

As of late, a three-dimensional microstructure-subordinate swelling model was produced for concentrating on the fission gas swelling kinetics in irradiated nuclear fuels. The model incorporated the rate theory (Booth model) and the Phase Field approach. We used the rate theory to represent the intra- and inter-granular gas bubble evolution, while we used the FP model to represent the impact of heterogeneous microstructures and inhomogeneous thermodynamic and kinetic properties on the generation and diffusion of fission items. Figure41 illustrates the impact of grain morphology on swelling kinetics obtained from this model. Figure41 below illustrates the impact of grain morphology on swelling kinetics obtained from this model.

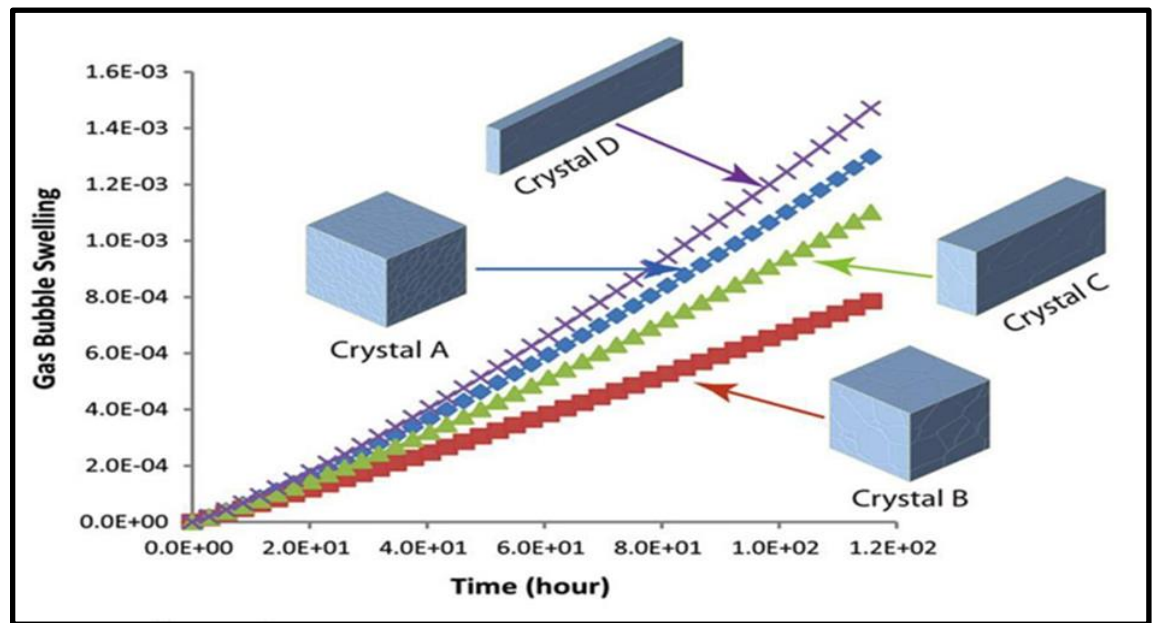


**Figure 41 Effect of grain morphology on gas bubble swelling kinetics under given fission rate  $\phi = 2.4 \times 10^{22}$  fission/cm<sup>3</sup>s and nucleation factor  $f_n = 0.02$ . Crystals A and B have average grain sizes of 1.34 μm, and 4.36 μm, respectively. Crystals B, C, and D have the similar average grain volume but different aspect ratios 1:1, 4:1, and 16:1 [12]**

In the simulation it was shown that both the decrease of grain size as well as the increase in grain aspect ratio accelerate swelling, and the hybrid model of rate theory and FP model provided a powerful simulation tool for engineering applications.

## **Chapter 5 - Conclusion**

We started with a general introduction and importance of simulation and applications of the Phase Field model in different areas. Then discussed the software and tools needed for simulations. After this the theoretical understanding about the phase separating alloys for understanding the spinodal region with the help of Cahn- Hilliard equation is studied. Coding and simulation part are done based on application of theory and microstructure is produced. Finally, the specific different applications of the Phase Field method are discussed.

## Chapter 6 -References

1. Phase Field Modelling NPTEL lectures by Prof.M.P. Gururajan, IIT Bombay
2. Porter, D. A., & Easterling, K. E. (2009). *Phase transformations in metals and alloys (revised reprint)*. CRC press
3. Tennyson, P. G., Kumar, P., Lakshmi, H., Phanikumar, G., & Dutta, P. (2010). Experimental studies and Phase Field modelling of microstructure evolution during solidification with electromagnetic stirring. *Transactions of Nonferrous Metals Society of China*, 20, s774-s780.
4. Sahoo, S., & Chou, K. (2016). Phase Field simulation of microstructure evolution of Ti–6Al–4V in electron beam additive manufacturing process. *Additive manufacturing*, 9, 14-24.
5. Ko, K. J., Cha, P. R., Park, J. T., Kim, J. K., & Hwang, N. M. (2007). Phase Field model simulation of grain growth in three dimensions under isotropic and anisotropic grain boundary energy conditions. In *Materials Science Forum* (Vol. 558, pp. 1101-1106). Trans Tech Publications Ltd.
6. Turret, D., Liu, H., & LLorca, J. (2022). Phase Field modelling of microstructure evolution: Recent applications, perspectives and challenges. *Progress in Materials Science*, 123, 100810.
7. Wang, Q., Zhang, G., Li, Y., Hong, Z., Wang, D., & Shi, S. (2020). Application of Phase Field method in rechargeable batteries. *npj Computational Materials*, 6(1), 1-8.

8. Zhao, Y., Xu, B. X., Stein, P., & Gross, D. (2016). Phase Field study of electrochemical reactions at exterior and interior interfaces in Li-ion battery electrode particles. *Computer methods in applied mechanics and engineering*, 312, 428-446.
9. Chen, L., Zhang, H. W., Liang, L. Y., Liu, Z., Qi, Y., Lu, P., ... & Chen, L. Q. (2015). Modulation of dendritic patterns during electrodeposition: A nonlinear Phase Field model. *Journal of Power Sources*, 300, 376-385.
10. Li, Y., Hu, S., & Stan, M. (2017). Application of the Phase Field method in predicting microstructure and property evolution of irradiated nuclear materials. *npjComput. Mater*, 3(16), 10-1038
11. Zacharie, I., Lansiart, S., Combette, P., Trotabas, M., Coster, M., & Groos, M. (1998). Microstructural analysis and modelling of intergranular swelling of an irradiated UO<sub>2</sub> fuel treated at high temperature. *Journal of nuclear materials*, 255(2-3), 92-104
12. Hu, S., Burkes, D., Lavender, C. A., & Joshi, V. (2016). Effect of grain morphology on gas bubble swelling in UMo fuels—A 3D microstructure dependent Booth model. *Journal of Nuclear Materials*, 480, 323-331.